Variable Thermal Emission from Aql X-1 in Quiescence

Robert E. Rutledge[1], Lars Bildsten[2], Edward F. Brown[3], George G. Pavlov[4], and Vyacheslav E. Zavlin[5]

ABSTRACT

We obtained four *Chandra*/ACIS-S observations beginning two weeks after the end of the November 2000 outburst of the neutron star (NS) transient Aql X$-$1. Over the five month span in quiescence, the X-ray spectra are consistent with thermal emission from a NS with a pure hydrogen photosphere and R_∞=15.9$^{+0.8}_{-2.9}$ (d/5 kpc) km at the optically implied X-ray column density. We also detect a hard power-law tail during two of the four observations. The intensity of Aql X$-$1 first decreased by 50$\pm$4% over three months, then increased by 35$\pm$5% in one month, and then remained constant ($<$6% change) over the last month. These variations in the first two observations cannot be explained by a change in the power-law spectral component, nor in the X-ray column density. Presuming that R_∞ is not variable and a pure hydrogen atmosphere, the long-term changes can only be explained by variations in the NS effective temperature, from $kT_{\mathrm{eff},\infty}$=130$^{+3}_{-5}$ eV, down to 113$^{+3}_{-4}$ eV, finally increasing to 118$^{+9}_{-4}$ eV for the final two observations. During one of these observations, we observe two phenomena which were previously suggested as indicators of quiescent accretion onto the NS: short-timescale ($<10^4$ sec) variability (at 32$^{+8}_{-6}$% rms), and a possible absorption feature near 0.5 keV. The possible absorption feature can potentially be explained as due to a time-variable response in the ACIS detector. Even so, such a feature has not been detected previously from a NS, and if confirmed and identified, can be exploited for simultaneous measurements of the photospheric redshift and NS radius.

[1] Department of Physics, Mathetmatics and Astronomy, California Institute of Technology, MS 130-33, Pasadena, CA 91125; rutledge@tapir.caltech.edu

[2] Institute for Theoretical Physics and Department of Physics, Kohn Hall, University of California, Santa Barbara, CA 93106; bildsten@itp.ucsb.edu

[3] Enrico Fermi Institute, University of Chicago, 5640 South Ellis Ave, Chicago, IL 60637; brown@flash.uchicago.edu

[4] The Pennsylvania State University, 525 Davey Lab, University Park, PA 16802; pavlov@astro.psu.edu

[5] Max-Planck-Institut für Extraterrestrische Physik, D-85748 Garching, Germany; zavlin@xray.mpe.mpg.de

Subject headings: stars: atmospheres — stars: individual (Aql X-1) — stars: neutron — x-rays: binaries

1. Introduction

Brown, Bildsten & Rutledge (1998, BBR98 hereafter) showed that the core of a transiently accreting neutron star (NS), such as Aql X-1 (for reviews of transient neutron stars, see Chen et al. 1997; Campana et al. 1998a), is heated to a steady-state temperature by nuclear reactions deep in the crust during the accretion outbursts. The timescale for the core to reach this steady-state is $\sim 10^4$ yr (see also Colpi et al. 2000), after which the NS emits a thermal luminosity in quiescence of (BBR98)

$$L_q = 8.7 \times 10^{33} \left(\frac{\langle \dot{M} \rangle}{10^{-10} M_\odot \mathrm{yr}^{-1}} \right) \frac{Q}{1.45 \mathrm{MeV}/m_p} \ \ \mathrm{ergs \ s}^{-1}, \tag{1}$$

where $\langle \dot{M} \rangle$ is the time-averaged mass-accretion rate onto the NS, and Q is the amount of heat deposited in the crust per accreted nucleon (Haensel & Zdunik 1990; see Bildsten & Rutledge 2000 for a discussion). Rutledge et al. (2001a, R01 hereafter) showed that, in the case of Aql X$-$1, the quiescent X-ray luminosity was within observational uncertainties of that predicted on the basis of its time-averaged accretion luminosity. This observation, and similar observations of other quiescent transient neutron stars (qNSs), strongly supports the scenario that deep crustal heating provides a "rock bottom" quiescent luminosity.

This quiescent thermal emission does not preclude that accretion onto the NS surface (at a rate $\dot{M}_c$) continues in quiescence at a substantially lower rate than during outburst. Narayan et al. (1997) argued that the analogous black hole (BH) systems accrete during quiescence via an advective flow that radiates inefficiently and makes quiescent BHs dim or non-detectable. This same accretion flow onto the NSs should be observable, with efficiencies $\epsilon = 0.20$ ($L_{\mathrm{X}} \sim \epsilon \dot{M}_c c^2$). Statistical comparisons show that the BHs are, on average, less luminous than NSs by a factor of ~ 10 (Barret & Vedrenne 1994; Narayan et al. 1997; Asai et al. 1998), although in individual cases they may be more luminous (V404 Cyg is an example of a BH which is more luminous than most qNSs; Kong et al. 2002). While this average difference in luminosity argues for a difference between the emission properties of NSs and of BHs, perhaps due to the presence of a surface in the former, detailed X-ray spectroscopy is still required to distinguish quiescent NSs from quiescent BHs in individual cases where the compact object mass is not measured nor type-I X-ray bursts observed (Rutledge et al. 2000).

Assessing the relevance of accretion as a source of the NS quiescent emission is hampered by the difficulty of predicting $\dot{M}_c$. In the context of an advection-dominated accretion flow (ADAF; Narayan & Yi 1994), $\dot{M}_c$ is set by the evaporation rate from the disk which is in turn related to the unknown disk truncation radius. Similar limitations apply for other low $\dot{M}$ solutions, such as the Adiabatic Inflow/Outflow Solution (ADIOS; Blandford & Begelman 1999). We are thus searching for direct indicators of quiescent accretion onto the NS: short term (timescales much less than the orbital period) intensity variability, and evidence of metals in the photosphere (BBR98; Bildsten & Rutledge 2000).

An intensity decrease of 40±8% across 5 yrs in Cen X-4 may well be explained as crustal cooling from a long ($\sim$100 yr) recurrence time NS (Rutledge et al. 2001c). Previous observations have shown shorter term variability ($\gtrsim$1 day). In Cen X-4 (Campana et al. 1997), the intensity decreased by a factor of $\sim$ 3 over 4 days[6] in 1997, approximately 18 years after the previous known outburst. Since, in crustal cooling variability, the timescale for variability scales with the time since the most recent outburst, four-day variability is much too short a timescale to occur 18 years post-outburst to be explained by this mechanism (Ushomirsky & Rutledge 2001).

A second means by which active accretion onto the NS would be indicated during quiescence is the presence of metals in the photosphere. For very low accretion rates (an order of magnitude estimate is $\dot{M}_c \ll 10^{-13}$ $M_\odot \mathrm{yr}^{-1}$) a transient NS will have a pure H atmosphere because the heavy element settling time is $\sim$ 10 s at the photosphere (Bildsten et al. 1992). At accretion rates above this, metals continuously populate the photosphere at such densities that their presence may be observable as absorption lines or edges (see Fig. 7).

Aql X-1 has been detected in X-ray quiescence six times: once with the *ROSAT*/HRI and twice with *ROSAT*/PSPC (Verbunt et al. 1994), once with *ASCA* (Asai et al. 1998), once with *BeppoSAX* (Campana et al. 1998b), and once with *Chandra* (R01). In all but the last (R01), the emission was interpreted as blackbody, although a significant power-law component was detected by Campana et al. (1998b), which dominated the emission above $\sim$2 keV, similar to a component observed from Cen X-4 (Asai et al. 1996a; Campana et al. 2000; Rutledge et al. 2001c). R01 examined a number of spectral models, discarding them in favor of a H atmosphere spectrum associated with emission from the NS photosphere.

We report here three additional *Chandra* detections in quiescence. In three of four

---

[6]Our re-analysis of the data found that the ROSAT/HRI countrate decreased by a factor of 4.1±0.6 over 4.4 days.

Chandra observations of Aql X−1 in quiescence, we detect neither short term variability, nor absorption lines; however, in the fourth observation, we detect both variability and a possible absorption line. While other explanations are not excluded, the presence of both short-term ($\lesssim 10^4$ sec) variability and absorption during the fourth observation, combined with the absence of both during the other three observations, is evidence for active accretion onto the NS in quiescence. The modest significance (5σ) of the absorption line does not permit detailed spectroscopic study; however, its presence— should it be confirmed with higher S/N observations—opens up the opportunity to measure the redshift at the NS photosphere. Simultaneous measurements of the redshift, which is a function of M/R, and R would constrain the NS equation of state.

We begin, in § 2, by reviewing the distance and reddening to Aql X−1. We then describe, in § 3, our observations, timing analysis, and spectral analysis. Section 4 discusses our interpretation of the spectra and its implications.

2. Aql X-1: Distance and Reddening

Callanan, Filippenko & Garcia (1999) showed that the optical counterpart to Aql X-1 is a faint star $0.46''$ from the previously mis-identified counterpart. This led to the counterpart's identification as a late type star (spectral type K7 to M0) with a quiescent magnitude $V = 21.6$ with reddening of $E(B - V) = 0.5 \pm 0.1$ (Chevalier et al. 1999). For standard conversions[7] ($A_V/E(B - V)$=3.1, Fitzpatrick 1999; N_H/A_V=1.79×10^{21} cm^{-2} mag^{-1}, Predehl & Schmitt 1995), this corresponds to an X-ray column density of $N_{H,22}$=0.28±0.06 (N_H=$N_{H,22}10^{22}$ cm^{-2}). Thorstensen et al. (1978) note that a nearby (1.4$'$) B-type star has an optical reddening $E(B - V)$=0.73 mag (no uncertainty given), implying $N_{H,22}$=0.40. These values are comparable to the integrated galactic HI measurements in the direction of Aql X−1 of $N_{H,22}$=0.34±0.01 (Dickey & Lockman 1990, from W3nH[8]; the uncertainty was found as $\sigma_{1\circ}/\sqrt{N}$, where $\sigma_{1\circ}$ is the dispersion of the N measurements within 1 degree, and $N = 7$). These N_H values are listed in Table 4. These values will be used for comparison with the results from spectral fitting in the following section.

The orbital period has been measured at $P_{\rm orb} = 18.95$ hr via photometric observations both in outburst (Chevalier & Ilovaisky 1998b; Garcia et al. 1999) and quiescence (Welsh et al. 2000). While Chevalier et al. (1999) estimated the distance to the binary as 2.5 kpc,

---

[7]The formal uncertainty in this conversion is 2%, however there are clear systematic deviations of 25% to factors of ∼few in some X-ray sources; this may be due in part to the assumed X-ray spectral model.

[8]http://heasarc.gsfc.nasa.gov

a re-examination of the arguments producing this distance (which neglected the need for Roche-lobe overflow in the primary) finds that it is between 4 and 6.5 kpc (R01); we adopt 5 kpc as our fiducial distance. This 20% uncertainty is neglected in our quoted uncertainties in R_∞, which only take into account the statistical uncertainty in our spectral fits. The system's orbital inclination is estimated to be $> 36°$ (Welsh et al. 2000).

3. Observations and Analysis

Aql X−1 was observed on four occasions, with identical instrumental set-up using the *Chandra*/ACIS-S detector, backside-illuminated chip. The X-ray source was placed $4'$ off-axis and the read-out limited to 1/8 of the chip area with time resolution of 0.44104 seconds; these settings mitigate pile-up to $< 1\%$ of the detected photons. In all observations, source counts were extracted from an 8 pixel radius about the source position; background was taken from an annulus of inner and outer radius of 10 and 50 pixels, respectively. The spacecraft roll angle differed between each observation. The X-ray source, however, fell on the same physical pixels which, due to the spacecraft dither (used to average over QE non-uniformity and bad pixels) and larger PSF, spanned ~ 50 detector pixels in both directions across the chip. In each of the four observations, the counts were centered near (`chipx, chipy`)=(690,710), with deviations between observations of ± 4 pixel; there are no known bad pixels within 50 pixels of this location. The expected background countrate in the source region was always $<1\%$. Analysis of the first of these observations is described elsewhere (R01). An observation list is in Table 1.

For the analysis we use CIAO 2.2.0.1 with CALDB 2.9; the ACIS-S3 chip calibration was improved in CALDB 2.7[9]; analyses of astrophysical sources shows no evidence of systematic deviations $>15\%$. However, the effects of a recently reported time dependence in the ACIS response is discussed in Sec. 3.4.

The first observation triggered as a Target of Opportunity, following the end of a bright X-ray outburst (see Fig. 1) – the brightest observed yet with RXTE/ASM (Jain et al. 2000; Rutledge 2000). The other three observations followed after a space of 2, 3 and 4 months from the first observation. The countrates in Table 1, in three separate passbands, show significant variability between observations 1, 2 and 3; observations 3 and 4 show identical countrates in all passbands. In the 0.5-10 keV passband, the countrate decreased by $51\pm8\%$ between observations 1 and 2 (over a period of 81 days), increased by $35\pm4\%$ between obs. 2 and 3 (across 32 days), and then remained consistent with constant ($\pm6\%$) across 28

---

[9]http://cxc.harvard.edu/cal/Links/Acis/acis/Cal_prods/matrix/matrix.html

days).

3.1. Short-Term ($<10^4$ sec) Variability

Using the same approach as in R01, we produced power density spectra (PDS) using all counts detected (no energy constraints, corresponding roughly to 0.2-10 keV) to search for broad-band variability (see Lewin et al. 1988 for the use of PDS in measuring broad-band variability in X-ray sources). We produced Fourier transforms of the time-series data, with time resolution of 0.44104 sec (Press et al. 1995). From these, we produced the PDS (the sum of the squares of the Fourier components as a function of frequency), and rebinned them logarithmically in frequency. The resulting PDS are shown in Fig. 2.

Visual examination of the PDS shows no evidence for broad-band power in observations 1-3 (there is marginally significant variability in observation 3, near 2×10^{-4} Hz); however, there is clear excess power at low frequencies during observation 4. We modeled the data as a power-law in frequency, plus a constant (Poisson) level ($P(\nu) = A\nu^{-\alpha} + C$); the best fit model gives a slope $\alpha = 1.8\pm0.4$ and an root-mean-square (RMS) variability of $32^{+8}_{-6}\%$, integrated between 0.0001-1 Hz (0.2-10 keV). Similar modeling to observations 1-3 (holding the power-law slope fixed at the best-fit value of observation 4) provide 3σ upper-limits between 18-29% rms during these observations (see Table 2). For comparison, we show the lightcurve of obs. 4 in Fig. 3. This is the first observation of short timescale ($< 10^4$ s) variability observed from the intrinsic spectrum of a quiescent NS transient (that is, not attributable to changes in the intervening X-ray column density).

We estimate (based on spectral fiting, below) that the power-law component only contributes 12% of the counts in the detector in the 0.2-10 keV energy range. This is insufficient to produce 32% variability. We conclude that the variability is in the thermal component.

Since the ratio of X-ray to bolometric luminosity $\log(L_X/L_{\rm bol})=0.5\pm0.2$ from Aql X$-$1 in quiescence is more than three orders of magnitude greater than observed from coronal emission from the analogous RS CVn systems (Bildsten & Rutledge 2000), we exclude the possibility that observed variability (at $\approx$30% of the quiescent luminosity) could be due to a coronal flare of the companion, since this would, again, be 3 orders of magnitude greater than flares seen from other systems (see also R01).

3.2. Spectral Analysis

Data were extracted, using *psextract*, into pulse-invariant (PI) spectra. We binned all spectral data identically, as shown in their best fit spectral figures (Figs 4a-d); the binning was selected so that: (1) low-energy bins are wider than the detector energy resolution; (2) the 0.45-0.60 keV bin integrates completely across the O-edge in the detector, over which the detection efficiency varies significantly; and (3) the high energy bins have comparable signal-to-noise. We analyzed the PI spectra using XSPEC v11.0.1 (Arnaud 1996).

Our default spectral model is a H atmosphere spectrum (Zavlin et al. 1996) plus power-law and galactic absorption[10]. Other spectral models (blackbody, Raymond-Smith plasma, pure power-law, disk blackbody) for this source in quiescence have been examined elsewhere (R01), using data from observation 1; note that in the present work, the analyzed data extends down to 0.3 keV, while in the previous work, data were not used below 0.5 keV.

We first fit the four spectra individually (§ 3.2.1), and followed this with combined fits of observations 1 and 2 (§ 3.2.2), and 3 and 4 (§ 3.2.3). This was done to address a systematic difference between the two groups of observations. We then attempted (§ 3.2.4) joint fits of all four observations to determine which spectral parameters changed between them.

3.2.1. Spectral Fits to the Individual Observations

We began by fitting all four spectra individually with an H atmosphere model with galactic absorption and no power-law component. While obs. 1 and 2 are statistically acceptably fit (reduced chi-squared statistic $\chi^2_\nu=2.05/10$ degrees of freedom, probability=0.03, $\chi^2_\nu=1.10/10$ dof, prob=0.36 respectively), obs. 3 and 4 are not ($\chi^2_\nu=4.23/10$ dof, prob=6×10^{-6}, $\chi^2_\nu=6.8/10$ dof, prob=10^{-10} respectively). Visual examination of the spectra from obs. 3 and 4 show systematic excesses in counts above the model prediction at energies >3 keV. Such an excess has been observed previously from this source (Campana et al. 1998b) and other qNSs (see § 4.2), and is typically modeled as a power-law component. We therefore include this component in all four spectral fits,

---

[10]Neutron star H atmosphere emergent spectral models—and more complicated metallic models—have also been calculated by Zavlin et al. (1996), Rajagopal & Romani (1996) and more recently by Gaensicke et al. (2002). The H atmosphere models of these three references agree to within ~few per cent at energies relevant to the present work, 0.1-3 keV.

to provide upper-limits on its flux in observations 1 and 2. The resulting best-fit spectral parameters for the individual observations are given in Table 3, and figures of the best-fit models and data are in Figs. 4a-d.

There is a systematic difference between the best-fit N_H value and R_∞ values between the pairs of observations 1+2 and 3+4. We address this in the following sections, by comparing first the spectra of observations 1 and 2, then the spectra of observations 3 and 4.

3.2.2. Observations 1 and 2

As neither of these spectra statistically require a power-law component, we investigate if the difference between them is due to N_H, $kT_{\rm eff,\infty}$, or R_∞. We jointly fit the two spectra with an absorbed H atmosphere plus power-law, permitting 1 of the three spectral parameters (N_H, $kT_{\rm eff,\infty}$, R_∞) to vary in turn between the two observations. We include a power-law component to avoid systematic bias in the derived H atmosphere spectral parameters. The resulting best-fit parameters and statistics are given in Table 5.

The hypothesis of a variable N_H is rejected. A variable R_∞ is statistically acceptable, although not physically motivated in the deep crustal heating model. Finally, the hypothesis of a variable $kT_{\rm eff,\infty}$ is statistically acceptable. We therefore attribute the difference between the spectra of these two observations to changes in the $kT_{\rm eff,\infty}$, which decreased from 125^{+12}_{-9} eV to 108^{+11}_{-7} eV over 81 days. These uncertainties include covariance with other spectral parameters (of which N_H and R_∞ are the strongest). When we hold all other parameters at their best-fit values, the uncertainties are 125 ± 1 eV, and 108^{+1}_{-2} eV (1 σ). Note that the best-fit $N_{\rm H,22}=0.43\pm0.03$ is consistent with values found through other methods (Table 4).

Attributing the variability to the magnitude of the power-law component is statistically permitted by the data; however, in so doing, the best-fit photon index is required to be steep (4.5 ± 0.2) as to necessarily dominate the emission across the full *Chandra* energy band ($>95\%$ of the 0.5-10 keV luminosity), the thermal component is not required statistically ($R_\infty<7.2$ km at a fiducial value of $kT_{\rm eff,\infty}=115$ eV), and the value of N_H is a factor of 2 above the optically implied value. As we know of no physical scenario in which such a steep power-law spectrum is produced, and it would require the luminosity to be serendipitously consistent with that of a NS with $R_\infty\approx15$ km at the observed distance and N_H, we think this hypothesis unlikely. We therefore attribute the different intensities of observations 1 and 2 to a change in $kT_{\rm eff,\infty}$.

3.2.3. Observations 3 and 4: A Possible Counts Deficit in the 0.45-0.6 keV Bin

We jointly fit observations 3 and 4 with the same absorbed H atmosphere plus power-law spectrum. A statistically acceptable fit is found (Table 5). Thus, Aql X$-$1 observations #3 and #4 are consistent with having the same spectrum and intensity. The best fit $N_{H,22}$ (0.60±0.05) is greater than that found by other methods (Table 4), including the value found from joint spectral fitting from observations 1 and 2. The value of R_∞ is marginally larger than in observations 1 and 2 (46^{+23}_{-11} km vs. $17.2^{+2.6}_{-3.6}$ km). In addition, the value of R_∞ is also larger than that found in a previous analysis of observation 1 alone (R01), in which we had used counts with energies >0.5 keV, and that found in analyses of *ROSAT* and *ASCA* data in which N_H was held fixed at the optically implied value (Rutledge et al. 1999).

When we hold $N_{H,22}$ and R_∞ fixed at the best-fit value from observations 1 and 2, the best-fit spectrum is marginally acceptable (χ^2_ν=1.71/25 dof, prob=0.015). Examination of the spectral model and data (Fig. 5) indicates a deficit in the 0.45–0.6 keV energy bin: the number of detected counts appears significantly below that predicted by the best fit model. When the 0.45–0.6 keV energy bin is removed from the fit, the new best-fit model is significantly improved (χ^2_ν=0.76/23 dof; prob=0.78). This suggests a deficit of counts in the 0.45–0.6 keV range in observations 3 and 4 (largely, the latter).

The best-fit model (ignoring this energy bin, with $N_{H,22}$ and R_∞ held fixed at the best-fit observation 1 and 2 values) predicts 20 and 25 counts in this bin for obs. 3 and 4 respectively (the difference in counts is due to different integration times). Only 14 and 10 counts are observed in observations 3 and 4. For an average countrate of 25 counts/bin, the Poisson probability of detecting ≤10 counts is 0.06%. Combining the two observations, the probability of detecting ≤24 counts (with an average of 45 counts/bin) is 0.04%. No such deficit is apparent in the spectra of observations 1 or 2.

3.2.4. Joint Fitting

To examine which spectral parameters are different between the four observations, we jointly fit all four spectra simultaneously. Because of the similarity between observations 3 and 4, we treat their spectra as being identical (i.e., all parameters for observations 3 and 4 are treated as the same), so we are examining the difference among three spectra, observations 1, 2 and 3+4. Table 6 contains a summary of our findings.

We fit the data with the absorbed H atmosphere + power-law spectrum and limited our fits to the 0.6–9.0 keV energy range, to avoid affects associated with the deficit below

0.6 keV in observation 4. As may be surmised from the different countrates, using a single spectrum with all five parameters ($N_{\mathrm{H},22}$, R_∞, α, $F_{X,pl}$, and $kT_{\mathrm{eff},\infty}$) free but the same for all 3 spectra, the best-fit is unacceptable (χ^2_ν=5.52/43 dof; prob=10^{-28}). We then allowed each of the spectral parameters to vary between observations.

1. A fit with $kT_{\mathrm{eff},\infty}$ allowed to vary is statistically acceptable, for values of $kT_{\mathrm{eff},\infty}$=121^{+13}_{-6} eV, 105^{+9}_{-6} eV, and 110^{+12}_{-5} eV for observations 1, 2, and 3+4 respectively. When we hold all other parameters fixed at their best-fit values (to exclude covariance in the uncertainties) the values are 121±1, 105±1, and 110±1 eV.

2. When we permit only N_{H} to vary between the three spectra, the best-fit is unacceptable (χ^2_ν=3.05/41 dof; prob=2×10^{-10}). Thus the changes between the spectra cannot be due only to a changing N_{H}.

3. Although not physically motivated, when we permit only R_∞ to vary between the three spectra, we obtain an acceptable fit (χ^2_ν=1.13/41 dof; prob=0.26). The range of acceptable R_∞ values is small: 12.5–17.6 km.

4. We then fit the data with only $F_{X,pl}$ allowed to vary. The best fit was not statistically acceptable (χ^2_ν=1.60/41 dof; prob=0.0085). When we permit both α and $F_{X,pl}$ to vary, the fit becomes acceptable; the changes between the power-law slopes are large, however, and the best-fit R_∞ is larger than expected from theory, and N_{H} is larger than that found through radio and optical observations. It is unlikely, therefore, that a variable power-law component is responsible for the different spectra.

The spectra of observations 1 and 2 are acceptably fit without a power-law component, and the combination of the three spectra are acceptably fit with only a changing $kT_{\mathrm{eff},\infty}$. This motivated a fit with the following parameters: no power-law component in observation 1 and 2; N_{H} held fixed at the radio measured value ($N_{\mathrm{H},22}$=0.34); R_∞ held fixed at 13.0 km (a value which nearly all theoretical EOSs can produce; Lattimer & Prakash 2001); and $kT_{\mathrm{eff},\infty}$ varying. The best-fit is acceptable (χ^2_ν=1.30/43 dof; prob=0.11). When we now expand the energy range of this fit to include 0.3–0.6 keV, however, the best fit becomes unacceptable (χ^2_ν=2.63/51 dof; prob=2×10^{-9}). Examination of the spectrum shows that the observed countrates are systematically lower than the predicted countrates in the 0.3–0.6 keV range. When we let both N_{H} and R_∞ float (with the same value in all three spectra), the best-fit spectral model is still not statistically acceptable (χ^2_ν=1.62/49 dof; prob=0.0038). This unacceptable spectral model is shown in Fig. 6. The most discrepant point is the 0.45–0.6 keV bin from observation 4. When this point is removed, a new best-fit model is acceptable (χ^2_ν=1.26/48 dof; prob=0.105).

Since the poor fit to the full data set can be attributed to the single low-energy bin in observation 4, one possibility is that N_{H} changed between observations 1+2 and observation 3+4. If we permit the values of N_{H} and $kT_{\mathrm{eff},\infty}$ to change between observation 1, 2 and 3+4, however, the spectrum is still not acceptably fit (χ^2_ν=1.66/47 dof; prob=3×10^{-3}); therefore, the deficit is not explained by a changing N_{H}.

In summary, the differences in the three spectra are acceptably explained as entirely due to a changing $kT_{\mathrm{eff},\infty}$ of the surface thermal emission. The differences cannot be explained as entirely due to either a changing power-law flux or to a variable N_{H}. While a combination of variability in α and $F_{X,pl}$ provides a statistically acceptable fit, the required variation in the power-law slope α is large and the resultant best-fit values of R_∞ and N_{H} are larger than we would *a priori* expect. *We therefore conclude that the simplest explanation for the variation in the spectrum of Aql X−1 in quiescence is due to a change in $kT_{\mathrm{eff},\infty}$ of a pure H atmosphere.*

3.3.   Re-examination of the Counts Deficit in Observation 4

We now turn our attention to the apparent deficit in counts in the 0.45–0.6 keV bin of observation 4. In particular, we examine whether it is possible to explain the deficit by some instrumental or analysis effect that is unrelated to the NS emission.

When we exchange the response matrix from obs. 4 to that from obs. 1, there is no effect on the spectral fit (the focal plane temperatures were the same in all observations, and the X-ray source was focussed at the same location on the S3 chip). The deficit is therefore not caused by a change in the calibrated spectral response particular to obs. 4.

What if the effective area of the 0.45-0.6 keV bin is simply different from that represented in CALDB v2.9? Could we simply change the expected number of counts (on the basis of the best-fit spectrum and the calibrated response) by the same constant factor, which would make all observed 0.45-0.6 keV countrate consistent with the expected number? The calibrated response is based on detailed knowledge of the telescope+detector system. We took the response matrix to be completely diagonal, such that a photon of energy E_n would be detected as a count with energy E_n. While the system response is considerably more complicated, with significant non-diagonal elements, this zeroth order approximation can reveal if change in the 0.45-0.6 keV effective area can account for the observed discrepancy, or if higher order changes would be necessary.

In Table 8, we list the number of counts detected in the 0.45-0.6 keV energy bin x_i during each observation i, and the number of counts predicted to be in the bin (μ_i) by our

best-fit spectral model (in which the 0.45–0.6 keV bin was ignored in observation 4). We then calculated a probability for the factor (f) by which we change the diagonal response,

$$Prob(f) = \Pi_{i=1}^4 P_{\text{Poisson}}(f \times \mu_i, x_i)$$

where $P_{\text{Poisson}}(\mu, x)$ is the Poisson probability of observing x_i counts when μ_i is the expected average realization. We find, for our observed and predicted values of x_i and μ_i, that $Prob(f)$ is maximal when $f = 0.75$ (that is, the observed counts would be most consistent with an effective area in the 0.45-0.6 keV bin which is 75% of the telescope+detector effective area represented in CALDBv2.9). We performed a Monte Carlo simulation, with 4 Poisson deviated counts, with mean counts of $f \times \mu_i$, calculating $Prob_{\text{Monte−Carlo}}(f = 0.75)$ for 10^6 such realizations. We found that we would produce a value of $Prob_{\text{MonteCarlo}}(f = 0.75) \leq Prob(f = 0.75)$ 2.0% of the time (that is, even the most likely value of f would produce the distribution of x_i observed only 2% of the time). We thus marginally exclude the counts deficit as due to a different effective area in the 0.45-0.6 keV bin from that in CALDB 2.9. To attribute the observed discrepancy to a response inaccuracy, there must either be a significant difference between a non-diagonal element as modelled and its true value, or the diagonal element response in the 0.45–0.6 keV bin (and only that bin) may be time dependent.

We also examined the spectrum in PHA space as well as PI space, and find the same deficit of counts in observation 4. A statistically anomalous background subtraction (i.e, more than an average number of background counts in this spectrum) is not responsible for the deficit either; when we neglect the background entirely (which we estimate to be ∼9 counts of the 1137 counts observed in this spectrum), the deficit remains.

We therefore marginally exclude the deficit of counts to response matrix uncertainty under a diagonal assumption, and exclude either anomalous background, or binning in PI space vs. PHA space. The deficit could be due to non-diagonal elements in the redistribution matrix being different than those in CALDB v2.9, or to an unknown time-dependency in the diagonal elements of the redistribution matrix.

3.4. Time Dependent Response Below 0.7 keV in ACIS-S3

When this work was largely complete, it was reported that there is a time-dependency in the response of the ACIS chips below 0.7 keV [11], which appears as a decrease in effective

---

[11]http://asc.harvard.edu/cal/Links/Acis/acis/Cal_projects/index.html

area, the magnitude of which has increased with time since launch. The magnitude, exact time dependency, and energy dependency are not fully known at present, and it is beyond the scope of the present work to provide a full time- and energy- dependent re-calibration effort. However, the discussed possible causes (deposition of contaminants on the CCDs or the optical blocking filter) suggest the effect would be monotonicaly increasing with time, perhaps at a constant rate.

We examined briefly the magnitude of this effect, to determine its possible effects on our conclusions. We used two observations of the spectrally soft super-nova remnant SNR E0102-72.3, taken 2000 May 28 (ObsID 141, ∼6 months prior to Obs. 1 of Aql X-1) and 2001 Dec 6 (ObsID 2844; ∼8 months after Obs. 4 of Aql X-1). These were taken with the same focal plane temperature ($-120F$) but at different locations on the ACIS-S3 chip (141 was 2.2′ off-axis, while 2844 was only 1′ off axis). We extracted data within 39″ of the SNR center, and produced pulse-invarint (PI) spectra with resolution (10-15 eV) greater than the intrinsic energy resolution of ACIS-S3 between 0.3-1.1 keV (120-140 eV). We modelled the first observation with a model meant to be parametric (`wabs * (c6vmekl + gauss)`), which with a best fit of χ^2_ν=3.30 for 32 dof was not statistically acceptable; however the most deviant PI bins were not systematically offset from the model (that is, the scatter appeared random as a function of energy), and were at most 3σ from the model. This is adequate for our purpose of investigating systematic response differences at the energy resolution of the detector.

We compared the second spectrum obtained 557 days later with the best-fit model of the first spectrum (see Fig. 8). As can be seen from the figure, the response appears to be diminished by ∼50% between 0.3-0.5 keV, with the magnitude of the discrepancy decreasing between 0.5-0.7 keV. Thus, from our comparison, we see an apparent change in the detector response, which may be modelled as an energy-dependent decrease in the effective area below 0.7 keV.

We investigate the effect of this on our conclusions regarding the broad-band spectrum, by using data only in the energy range 1-10 keV. First, as can be seen from Table 1, the 1.0-2.5 and 2.5-8 keV countrates vary between observations, and so cannot be explained as due to the <1 keV response. Joint spectral fits using all four observations still find that the variation cannot be explained as due to a change in N_H or power-law component normalization alone (both with values of χ^2_ν with corresponding probabilities of $<10^{-3}$). Since we are simply removing data from consideration, all those combinations of parameters which produced acceptable spectral fits using 0.3-10 keV still produce acceptable fits using 1-10 keV, but with larger error bars. Thus, the conclusion that the observation-to-observation variability is explained by a change in $kT_{\rm eff,\infty}$ remains. We

expect the time-dependent calibration of the sub-1 keV range, when it is fully known, will change the resulting spectral parameters we have measured here, but not our qualitative conclusions.

Finally, as regards the apparent counts deficit, the change in effective area does affect the energy range of interest (0.45-0.6 keV). We performed the following check. First, using the E0102-72.3 observations, we included a multiplicative `spline` model in XSPEC to account for the change in calibration; this was done by first finding the best-fit parametric model to the May '00 observation only, and using the same parameters held frozen for the Dec '01 data, but including a `spline` model, with Estart=0.3 keV, Eend=0.7 keV, Yend=1.0, YPend=0.0, and the values of Ystart and YPstart permitted to vary. The best-fit spectrum was unacceptable (χ^2_ν=15.3, 52 dof), although the gross change in response was well accounted for, with best-fit values of Ystart=1.5 and YPstart=−20. We then refit Obs. 1-4 with the spectral model which had been previously unacceptable due to the counts deficit ($kT_{\mathrm{eff},\infty}$ varies between observations, N_{H} and R_∞ permitted to float, and a power-law spectral component for Obs. 3 and 4 only), but including the spline component for Obs 3 and 4. This models the change in response as essentially instantaneous between observations 2 and 3. The best-fit joint spectrum is statistically acceptable, and the deficit is no longer significant (χ^2_ν=1.23 / 49 dof; prob=0.13). The accuracy of this correction, however, depends in detail on the time-dependence of the change in response, and whether or not it can be modelled as a change in effective area as a function of energy. This requires much more detailed modelling of the response than we can do here. We conclude, however, that the deficit of counts can be due entirely to the change in detector response; this requires confirmation through detailed study and modelling on the time- and energy-dependence of the sub-0.7 keV detector response.

4. Discussion and Conclusions

Following an outburst of Aql X−1 during November 2000, we took four *Chandra*/ACIS-S snapshots over a span of 5 months. With this series of spectra, we find the following.

1. All four spectra are acceptably fit with H photosphere models, with radii consistent with that of a NS, at the distance and reddening of Aql X-1. In two of the four spectra, an additional power-law component is required to acceptably fit the spectrum at high energies (>3 keV), as has been found previously for this and other qNSs.

2. The intensity decreased by 50% over the first three months following the outburst. It then increased by 35% over the next month and then remained constant for the

last month spanned by our observations. The change in the spectrum between the observations cannot be explained exclusively as a change in the power-law component, nor in the value of N_{H}. A change in the photospheric effective temperature is required to account for the change.

3. No short timescale ($< 10^4$ s) variability was found in the first three observations; the fourth had significant variability ($32^{+8}_{-6}\%$ rms, 0.2-10 keV) on timescales 10^3–10^4 sec. As the power-law component contributes a smaller fraction ($\sim 12\%$) to the total counts, this magnitude in variability cannot be attributed to the power-law component.

4. A deficit of counts in the 0.45–0.6 keV band was noted during observation 4. This deficit was not present in the other three observations. Follow-up spectroscopy and detailed study of the change in the detector response is required to determine if the deficit is intrinsic to the source.

5. A best-fit spectral model, excluding the 0.45-0.6 keV bin in observation 4, gives a value of $N_{\mathrm{H,22}}=0.42^{+0.02}_{-0.03}$ – consistent with the optical and radio implied value; the best fit $R_\infty=15.9^{+0.8}_{-2.9}$ km (neglecting the 20% uncertainty in the 5 kpc distance), consistent with the radius of a NS for most proposed NS EOS (Lattimer & Prakash 2001).

The increase in temperature between observations 2 to 3, if significant, is interesting. While accretion can clearly affect the thermal spectrum (e.g., Zampieri et al. 1995), it is also possible that differential sedimentation of ions in the atmosphere can change the surface effective temperature by modifying the opacity at intermediate densities, $10^5 \; \mathrm{g\,cm^{-3}} \lesssim \rho \lesssim 10^8 \; \mathrm{g\,cm^{-3}}$, (Brown et al. 2002). Further detailed calculations are required to determine the amplitude and timescale of this effect.

At present, there is no known mechanism associated with crustal heating that can produce the short-timescale ($\lesssim 10^4$ sec) variability we observe here. The minimum timescale for post-outburst intensity variability in quiescence from deep crustal heating is days to months (the thermal diffusion timescale from the depth of heat deposit), and should scale roughly as δt, where δt is the time since a (short) outburst ends (Ushomirsky & Rutledge 2001). For NSs with "normal" cores, the magnitude of variability is a few per cent; if more exotic neutrino cooling takes place in the core, however, the magnitude of variability in quiescence can be a factor of ten or more. In the absence of variability due to post-outburst crustal cooling, the only other timescale for variability is the timescale of core cooling, which is typically 10^5–10^6 yr. In contrast, intensity variability due to accretion onto the compact object can in principle take place on the dynamical timescale, seconds or shorter. However, while the observation is in qualitative agreement with accretion onto

the compact object, it remains a major puzzle why the magnitude of luminosity should be quantitatively comparable to the luminosity predicted previously from deep crustal heating R01. The absence of a quantitative prediction for the magnitude of accretion onto the compact object in quiescence further complicates comparison between this observation and an accretion theory. For the present, we conclude that the intensity variability on $<10^4$ sec timescale can be explained by accretion onto the compact object, but the implied coincidence of the accretion luminosity being comparable to the predicted deep crustal heating luminosity, as found by R01, remains a challenge to theory.

4.1. Uncertainties in the Measurement of R, and Prospects for a Useful Constraint on the EOS

Throughout this paper, we use the word "radius" to mean the measured value R_∞, the effective emission area size observed from an infinite distance. In practice, what we measure using spectral analysis is the angular size of the source R_∞/D, where D is the distance to the NS. We assume $D =$5kpc, a value which is at present uncertain by $\pm20\%$ (R01); we neglect this uncertainty throughout the present work, addressing only the statistical and spectral uncertainty, which can be greatly improved upon with higher signal-to-noise X-ray spectra. The distance to Aql X$-$1 can be accurately measured in the future using the Space Interferometry Mission (SIM; Unwin 1998), which can achieve $\pm2\%$ accuracy at 5 kpc for an object with $V < 17m$ (Aql X-1 obtains $V = 14.8$ in outburst ; Liu et al. 2001). Such precise measurement will effectively eliminate distance as an uncertainty in R_∞. Indeed, using spectral analyses of qNSs in globular clusters (Grindlay et al. 2001; Rutledge et al. 2001b; in't Zand et al. 2001), the distances to which can be measured with $\pm2\%$ precision using Hipparcos dwarfs (Carretta et al. 2000), is one approach being pursused to obtain accurate R_∞ measurements prior to the launch of SIM.

We have assumed throughout this work that R_∞ does not change. In the deep crustal heating scenario (BBR98), luminosity originates from the NS core, and the NS star has a $kT_{\text{eff},\infty}$ which is isotropic at the photosphere, which we assume throughout this paper. This scenario, however, is not entirely consistent with the short-term (seconds-months) variability which is observed. If the photosphere were to have temperature anisotropies – for example, which may occur if the NS were powered exclusively by non-spherically symmetric accretion – this would change the physical meaning of R_∞, which would then dependent on the details of the photospheric temperature distribution, as described for accreting NSs at much higher luminosities than are relevant here (Psaltis et al. 2000).

The value of R_∞ is related to the physical radius R by $R_\infty=R/\sqrt{1 - 2GM/(Rc^2)}$,

where G is the graviational constant, M is the NS mass, and c is the speed of light. It is the value R which has recently been shown to place a useful constraint on the NS EOS (Lattimer & Prakash 2001), if R is measured to $\lesssim 10\%$ accuracy. The value R cannot be derived from R_∞ in the absence of a known NS mass M. If one assumes a range of values between 0.8-2.8$M_\odot$, this introduces an additional systematic uncertainty of $\sim 50\%$ in R, which is greater than that needed to usefully constrain the EOS in the prescription of Lattimer & Prakash (2001). Thus, precise measurements of R_∞ will not usefully constrain the NS EOS in the absence of a measured NS mass or photospheric redshift; however, if a phenomenological relationship between R_∞ and the pressure at nuclear density for a range of EOSs can be found, as found for R by Lattimer & Prakash (2001), it may be that R_∞ will usefully constrain the NS EOS. This possibility is presently under examination.

4.2. The Power Law Component

A power-law spectral component is required to fit the spectrum above 3 keV in 2 of the four observations, and it is consistent with being the same magnitude and slope in all four observations.

A high energy power-law tail has now been observed to dominate the X-ray spectrum above 2-3 keV in five qNSs: Aql X-1, Cen X−4 (Asai et al. 1996b; Campana et al. 2000; Rutledge et al. 2000), KS 1731-260 (Wijnands et al. 2001; Rutledge et al. 2002), NGC 6440 (in't Zand et al. 2001) and 4U 2129+47 (Nowak 2002). In all cases, this component comprises $\sim$10-40% of the 0.5-10 keV luminosity. Importantly, in all those power-law components which have been detected, the slope appears to be either inverted or flat. A cutoff at higher photon energies (above 3 keV) is required for the luminosity not to diverge.

It has previously been suggested that the component may be due to accretion onto the NS magnetosphere (Campana et al. 1998a); however, no detailed *a priori* model (including an energy budget, estimation of the accretion rate onto the compact object or magnetosphere) exists. If the power-law emission were powered by accretion onto the magnetosphere, however, it would be coincidental that five different sources (each having different B fields, spin rates, and perhaps accretion rates onto the magnetosphere) would have comparable luminosity ratios of the power-law component to the thermal component, which originates from the NS surface. The same coincidence would apply to non-thermal emission from pulsar shocks as well (Tavani 1991; Stella et al. 1994; Menou et al. 1999).

One possible suggestion is that both the thermal and power-law spectral components are powered by low-level accretion. Using the assumption of spherical flow onto an

unmagnetized, nonrotating neutron star, and assuming that only Coulomb forces acted to decelerate the infalling protons, Zampieri et al. (1995) showed that no similarly hard spectral component was expected at accretion rates comparable to that required to power the quiescent thermal emission. Deufel et al. (2001) similarly found that, for accretion via an advective flow with virialized protons, the emergent spectrum is slightly harder than thermal, though the hardened component still decreases in νF_ν. It is therefore unclear that the emergent spectrum of a low $\dot{M}$ NS would produce a hard tail such as observed here.

4.3. A Deficit of Counts in the 0.45-0.6 keV Bin in Observations 3 and 4

We found that, compared with a spectral model interpolation in the 0.45-0.6 keV energy range, there is a deficit of counts significant at the 99.96% level, during observations 3 and 4. Such a deficit is not present in observations 1 or 2. There are at least a few possible explanations for this.

It may simply be that the deficit is a statistical anomaly, which will not be confirmed with deeper spectroscopy. We may be able to address this possibility with our approved 30ksec AO-1 GO observation of Aql X−1 with XMM-Newton.

A simple decrease in the effective area in the 0.45-0.6 keV energy bin, by a factor of 0.75, is marginally excluded (2% probability) as the source of the counts deficit. The deficit may be due, however, to non-diagonal elements of the photon energy redistribution matrix which are different from those in the present calibration model. Moreover, a recently reported time-dependence in the ACIS response below 0.7 keV can expalain the entire deficit, when the time dependence of the change in response is modelled as having taken place between Feb and April 2001 (observations 2 and 4). Until this response is properly modelled, it cannot be neither fully implicated nor exonerated as being responsible for the counts deficit. Thus, an unaccounted-for discrepancy in the detector response remains a possible explanation.

Finally, it may be that the deficit of counts is due to the presence of metals. This would be consistent with the observational scenario expected to produce such features (Brown et al. 1998), in which active accretion onto the NS surface replenishes the surface metallicity. The detected intensity variability ($32^{+8}_{-6}\%$ rms) argues for active accretion during this observation as well (such variability may also be present during observation 3); and the luminosity of Aql X−1 during these observations is consistent with this scenario as well.

We show in Fig. 7 the emergent spectra of a solar-metallicity atmosphere from a NS

with the effective temperature of Aql X−1, rotating at 550 Hz (Zhang et al. 1998), at three different viewing angles with respect to the rotation axis (the orbital plane of Aql X−1, is $\alpha > 36°$). The absorption features due to metallic absorption lines are apparent in the pole-on ($\alpha = 0°$) spectral model. The most prominent feature, smeared by NS rotation, is near 0.9 keV, which is a mixture of OVII absorption, plus other metal absorption lines. In a rough approximation: to redshift this feature to 0.45-0.6 keV requires a redshift $1 + z = g_r^{-1} = 1/\sqrt{1 - 2GM/(Rc^2)}$=1.5-2.0, which, for a NS of $R_\infty = Rg_r^{-1}$=15.9 km, implies a coordinate radius $R = 8 - 10.5$ km, and a mass $M \approx 2.0M_\odot$. This is a mass/radius estimate of scale, which shows consistency with theoretical expectations, but is not a precise estimate due to the large uncertainty in the redshift factor, in addition to the systematic uncertainty in the correct identification and reality of the feature in question.

If future observations confirm the presence of this absorption line in Aql X−1 in quiescence, it can be exploited. By measuring the redshift of such lines (g_r^{-1}) simultaneously with the emission area from the spectrum ($\propto R^2 g_r^{-2}$) the NS mass and radius can be determined, providing a strong constraint on the equation of state of dense matter (Lattimer & Prakash 2001).

References

Arnaud, K. A., 1996, in G. Jacoby & J. Barnes (eds.), *Astronomical Data Analysis Software and Systems V.*, Vol. 101, p. 17, ASP Conf. Series

Asai, K., Dotani, T., Hoshi, R., Tanaka, Y., Robinson, C. R., & Terada, K., 1998, PASJ 50, 611

Asai, K., Dotani, T., Kunieda, H., & Kawai, N., 1996a, PASJ 48, L27

Asai, K., Dotani, T., Mitsuda, K., Hoshi, R., Vaughan, B., Tanaka, Y., & Inoue, H., 1996b, PASJ 48, 257

Barret, D. & Vedrenne, G., 1994, ApJS 92, 505

Bildsten, L. & Rutledge, R. E., 2000, *The Neutron Star – Black Hole Connection*, Kouveliotou et al (eds.) (NATO ASI Elounda 1999); astro-ph/0005364

Bildsten, L., Salpeter, E. E., & Wasserman, I., 1992, ApJ 384, 143

Blandford, R. D. & Begelman, M. C., 1999, MNRAS 303, L1

Brown, E. F., Bildsten, L., & Chang, P., 2002, ApJ, submitted

Brown, E. F., Bildsten, L., & Rutledge, R. E., 1998, ApJ 504, L95, [BBR98]

Callanan, P. J., Filippenko, A. V., & Garcia, M. R., 1999, IAU Circ. 7086

Campana, S., Colpi, M., Mereghetti, S., Stella, L., & Tavani, M., 1998a, A&A Rev. 8, 279

Campana, S., Mereghetti, S., Stella, L., & Colpi, M., 1997, A&A 324, 941

Campana, S., Stella, L., Mereghetti, S., Colpi, M., Tavani, M., Ricci, D., Fiume, D. D., & Belloni, T., 1998b, ApJ 499, L65

Campana, S., Stella, L., Mereghetti, S., & Cremonesi, D., 2000, A&A 358, 583

Carretta, E., Gratton, R. G., Clementini, G., & Fusi Pecci, F., 2000, ApJ 533, 215

Chen, W., Shrader, C. R., & Livio, M., 1997, ApJ 491, 312

Chevalier, C. & Ilovaisky, S. A., 1998a, A&A 330, 201

Chevalier, C. & Ilovaisky, S. A., 1998b, IAU Circ. 6806

Chevalier, C., Ilovaisky, S. A., Leisy, P., & Patat, F., 1999, A&A 347, L51

Colpi, M., Geppert, U., & Page, D., 2000, ApJ 529, L29

Deufel, B., Dullemond, C. P., & Spruit, H. C., 2001, å, accepted, astro-ph/0108438

Dickey, J. M. & Lockman, F. J., 1990, ARA&A 28, 215

Fitzpatrick, E. L., 1999, PASP 111, 63

Gaensicke, B. T., Braje, T. M., & Romani, R. W., 2002, A&A

Garcia, M. R. & Callanan, P. J., 1999, AJ 118, 1390

Garcia, M. R., Callanan, P. J., McCarthy, J., Eriksen, K., & Hjellming, R. M., 1999, ApJ 518, 422

Grevesse, N. & Noels, A., 1993, in E. Prantzos, M. Vaugioni-Flam, & M. Gasse (eds.), *Origin and Evolution of the Elements*, p. 14, Cambridge University Press

Grindlay, J. E., Heinke, C., Edmonds, P. D., & Murray, S. S., 2001, *Science* 292, 2290

Haensel, P. & Zdunik, J. L., 1990, A&A 227, 431

in't Zand, J. J. M., van Kerkwijk, M. H., Pooley, D., Verbunt, F., Wijnands, R., & Lewin, W. H. G., 2001, ApJ 563, L41

Jain, R., Bailyn, C., Coppi, P., Garcia, M., Levine, A., Orosz, J., Lu, P., Espinoza, J., & Gonzalez, D., 2000, IAU Circ. 7495

Kong, A. K. H., McClintock, J. E., Garcia, M. R., Murray, S. S., & Barret, D., 2002, ApJ, submitted, astro-ph/0111134

Lattimer, J. M. & Prakash, M., 2001, ApJ 550, 426

Leahy, D. A., Darbro, W., Elsner, R. F., Weisskopf, M. C., Kahn, S., Sutherland, P. G., &

Grindlay, J. E., 1983, ApJ 266, 160

Lewin, W. H. G., Van Paradijs, J., & Van der Klis, M., 1988, *Space Science Reviews* 46, 273

Liu, Q. Z., van Paradijs, J., & van den Heuvel, E. P. J., 2001, A&A 368, 1021

Menou, K., Esin, A. A., Narayan, R., Garcia, M. R., Lasota, J. P., & McClintock, J. E., 1999, ApJ 520, 276

Narayan, R., Garcia, M. R., & McClintock, J. E., 1997, ApJ 478, L79

Narayan, R. & Yi, I., 1994, ApJ 428, L13

Nowak, M., 2002, preprint

Predehl, P. & Schmitt, J. H. M. M., 1995, A&A 293, 889

Press, W., Flannery, B., Teukolsky, S., & Vetterling, W., 1995, *Numerical Recipies in C*, Cambridge University Press

Psaltis, D., Özel, F., & DeDeo, S., 2000, ApJ 544, 390

Rajagopal, M. & Romani, R. W., 1996, ApJ 461, 327

Rutledge, R. E., 2000, *The Astronomer's Telegram* 63

Rutledge, R. E., Bildsten, L., Brown, E. F., Pavlov, G. G., & Zavlin, V. E., 1999, ApJ 514, 945

Rutledge, R. E., Bildsten, L., Brown, E. F., Pavlov, G. G., & Zavlin, V. E., 2000, ApJ 529, 985

Rutledge, R. E., Bildsten, L., Brown, E. F., Pavlov, G. G., & Zavlin, V. E., 2001a, ApJ 559, 1054 [R01]

Rutledge, R. E., Bildsten, L., Brown, E. F., Pavlov, G. G., & Zavlin, V. E., 2001b, ApJ, submitted, astro-ph/0105405

Rutledge, R. E., Bildsten, L., Brown, E. F., Pavlov, G. G., & Zavlin, V. E., 2001c, ApJ 551, 921

Rutledge, R. E., Bildsten, L., Brown, E. F., Pavlov, G. G., Zavlin, V. E., & Ushomirsky, G., 2002, ApJ, submitted, astro-ph/0108125

Stella, L., Campana, S., Colpi, M., & Mereghetti, S. andx Tavani, M., 1994, ApJ 423, L47

Tavani, M., 1991, ApJ 379, L69

Thorstensen, J., Charles, P., & Bowyer, S., 1978, ApJ 220, L131

Unwin, S. C., 1998, in *Exozodiacal Dust Workshop, p. 291*, p. 291, see also http://sim.jpl.nasa.gov/

Ushomirsky, G. & Rutledge, R. E., 2001, MNRAS 325

Verbunt, F., Belloni, T., Johnston, H. M., Van der Klis, M., & Lewin, W. H. G., 1994, A&A 285, 903

Welsh, W. F., Robinson, E. L., & Young, P., 2000, AJ 120, 943

Wijnands, R., Miller, J. M., Markwardt, C., Lewin, W. H. G., & van der Klis, M., 2001, ApJ 560, L159

Zampieri, L., Turolla, R., Zane, S., & Treves, A., 1995, ApJ 439, 849

Zavlin, V. E., Pavlov, G. G., Sanwal, D., Manchester, R. N., Trümper, J., Halpern, J. P., & Becker, W., 2002, ApJ

Zavlin, V. E., Pavlov, G. G., & Shibanov, Y. A., 1996, A&A 315, 141

Zhang, W., Jahoda, K., Kelley, R. L., Strohmayer, T. E., Swank, J. H., & Zhang, S. N., 1998, ApJ 495, L9

Fig. 1.— Lightcurve of Aql X-1, outburst through quiescence. $RXTE$/ASM points (squares) used the ASM countrates, assuming 1 ASM c/s=4.4×10^{-10} erg cm^{-2} s^{-1} (0.5-10 keV; appropriate for a $kT = 5$ keV thermal bremsstrahlung spectrum corrected for absorption), and the ACIS-S points (triangles) assume the spectrum for observations 3 and 4 (1 ACIS-S c/s=1.0×10^{-11} erg cm^{-2} s^{-1}, 0.5-10 keV). Only ASM detections of $> 4\sigma$ are used. The uncertainty in luminosity due to the countrate is shown; the uncertainty in luminosity does not include the systematic uncertainty in the bolometric correction.

Fig. 2.— PDS of observations 1-4. Points are data, normalized according to Leahy et al.(1983). Error bars and upper-limits are 1σ. Solid lines are the best-fit broad-band models (see text). RMS variability model values are 0.0001-1 Hz, for all counts data detected (roughly, 0.2-10 keV). Observations 1-3 give only upper-limits for variability, while in observation there is a clear detection of variability, with $32^{+8}_{-6}\%$ rms.

Fig. 3.— Lightcurve of observation 4.

Fig. 4.— Best fit spectra for observations 1–4 (parameters are in Table 3). Crosses are the observed data. The dashed line is the thermal component, the dashed-dotted line is the power-law component, and the solid line is the summed spectral model; the spectral models have been corrected for galactic absorption. (a) Obs. 1. (b) Obs. 2. (c) Obs. 3. (d) Obs. 4.

Fig. 5.— (Top Panel) The observed spectra for observations 3 (open squares) and 4 (open circles), and the best-fit model in which the column density is held fixed at $N_{H,22}$=0.38 – the best-fit value from observations 1 and 2, as well as comparable to the optically implied value ($N_{H,22}$=0.35). The spectrum is statistically unacceptable, due to the deficit of counts in the 0.45-0.6 keV bin. (Bottom Panel) The residuals χ=(data-model)/uncertainty.

Fig. 6.— (Top Panel) Observations 1–4, with an (unacceptable) best spectral fit (see text), due to the low countrate in the 0.45-0.6 keV bin of observation 4. Observation 1 (stars), 2 (triangles), 3 (squares), and 4 (circles). (Bottom Panel) Residuals χ=(data-model)/uncertainty.

Fig. 7.— The emergent (top of the atmosphere – that is, un-redshifted) X-ray spectrum for a NS atmosphere ($1.4 M_{\odot}$, 10km) of solar metallicity including the effects of a NS rotating at 550 Hz, as observed from Aql X−1, at three viewing angles (α) relative to the direction of NS rotation. The solid line, in which absorption features are apparent, is for an angle $\alpha = 0$ of the NS rotation axis relative to the line of sight. The broken line is for $\alpha = 30°$, and the smooth solid curve us for $\alpha = 90°$. Z indicates the percentage of metals, assuming the mixture of Grevesse and Noels (1993). For Aql X−1 the best estimate of the rotational inclination is $\alpha > 36°$.

Fig. 8.— **Top Panel**: Comparison of two X-ray spectra for the soft SNR E0102-72.3 between 0.3 and 1.1 keV, taken 5 May 2000 (crosses) and 6 Dec 2001 (boxes). A parametric model (solid line) is fit to the the May '00 observation. The Dec '01 spectrum is systematically below the May '00 at energies 0.3-0.7 keV. (**Bottom panel**) Ratio of the best-fit May '00 parametric spectral model to the May '00 (crosses) and Dec '01 (boxes) data. The systematic difference in spectra shows a strong energy dependence: approximately 50% near 0.3-0.5 keV, increasing to consistency (100%) near 0.7 kev. Comparison of the increases and decreases in the PI spectra also indicate a possible gain shift between the two observations, by ∼10 eV.
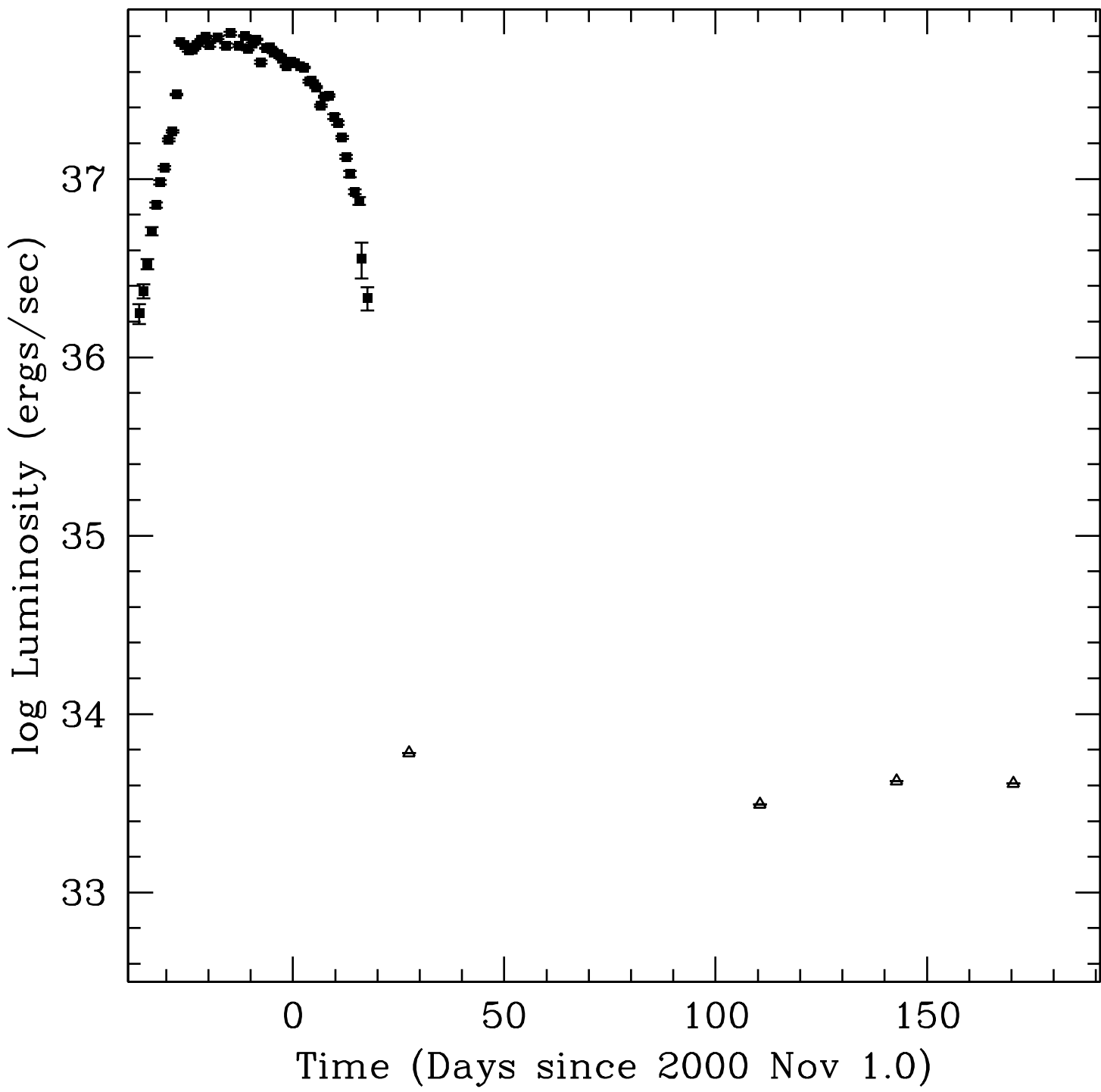
Figure 1
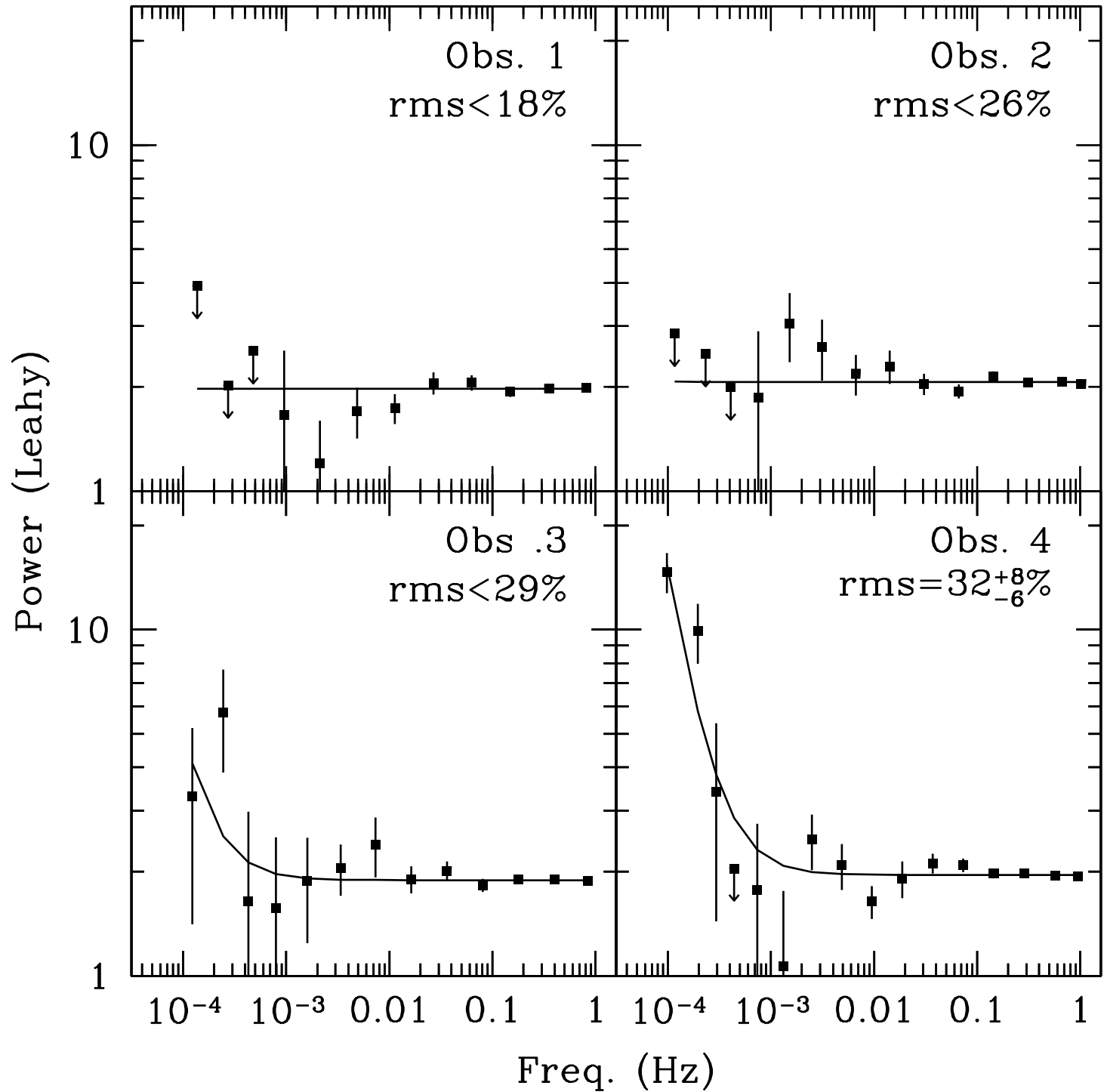
Figure 2
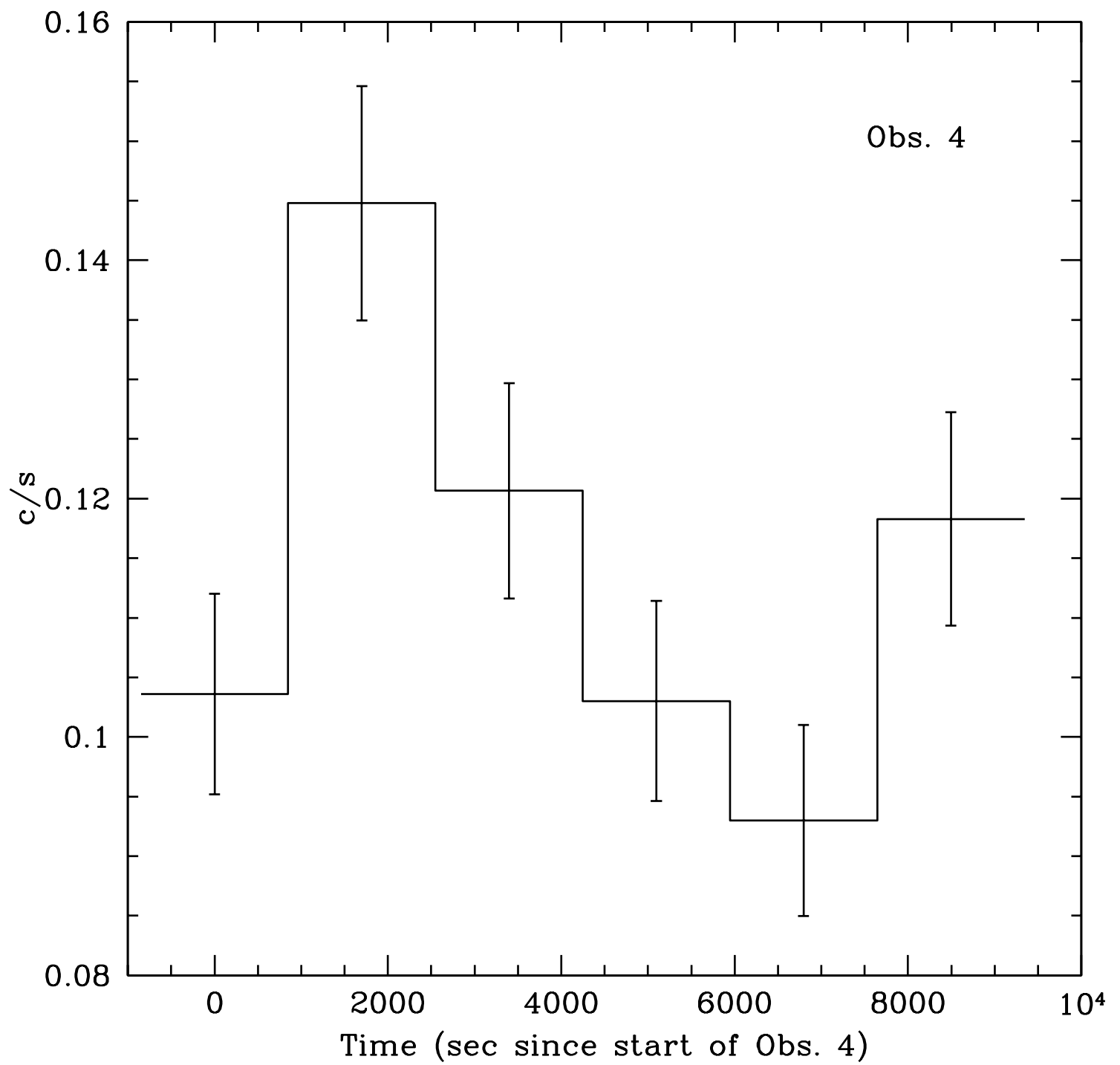
Figure 3

Aql X−1, Nov 28 2000: Chandra ACIS−S/BI

Energy (keV)

keV cm^{-2} s^{-1}
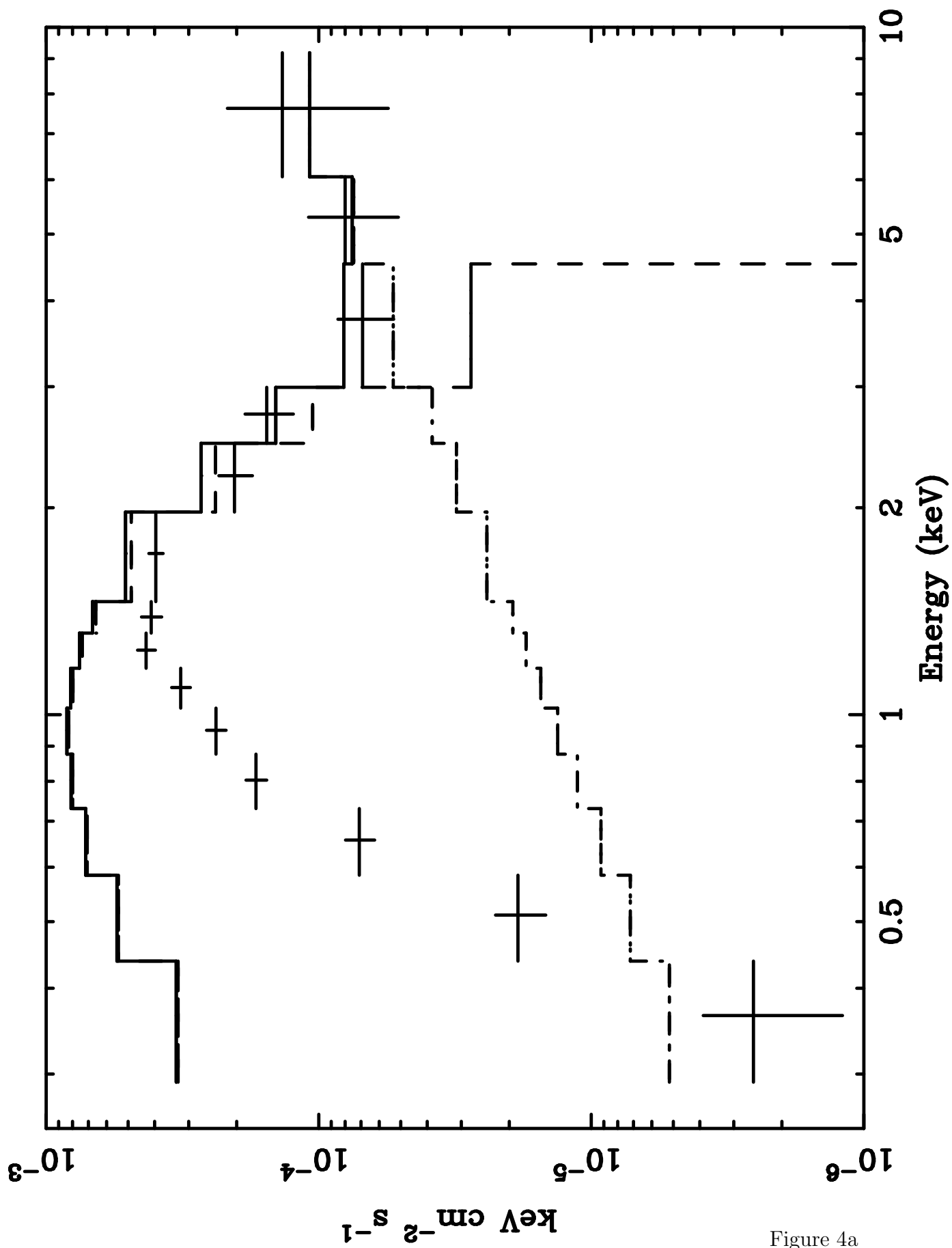
Figure 4a

Aql X-1, Feb 19 2001: Chandra ACIS-S/BI

keV cm^{-2} s^{-1}

Energy (keV)
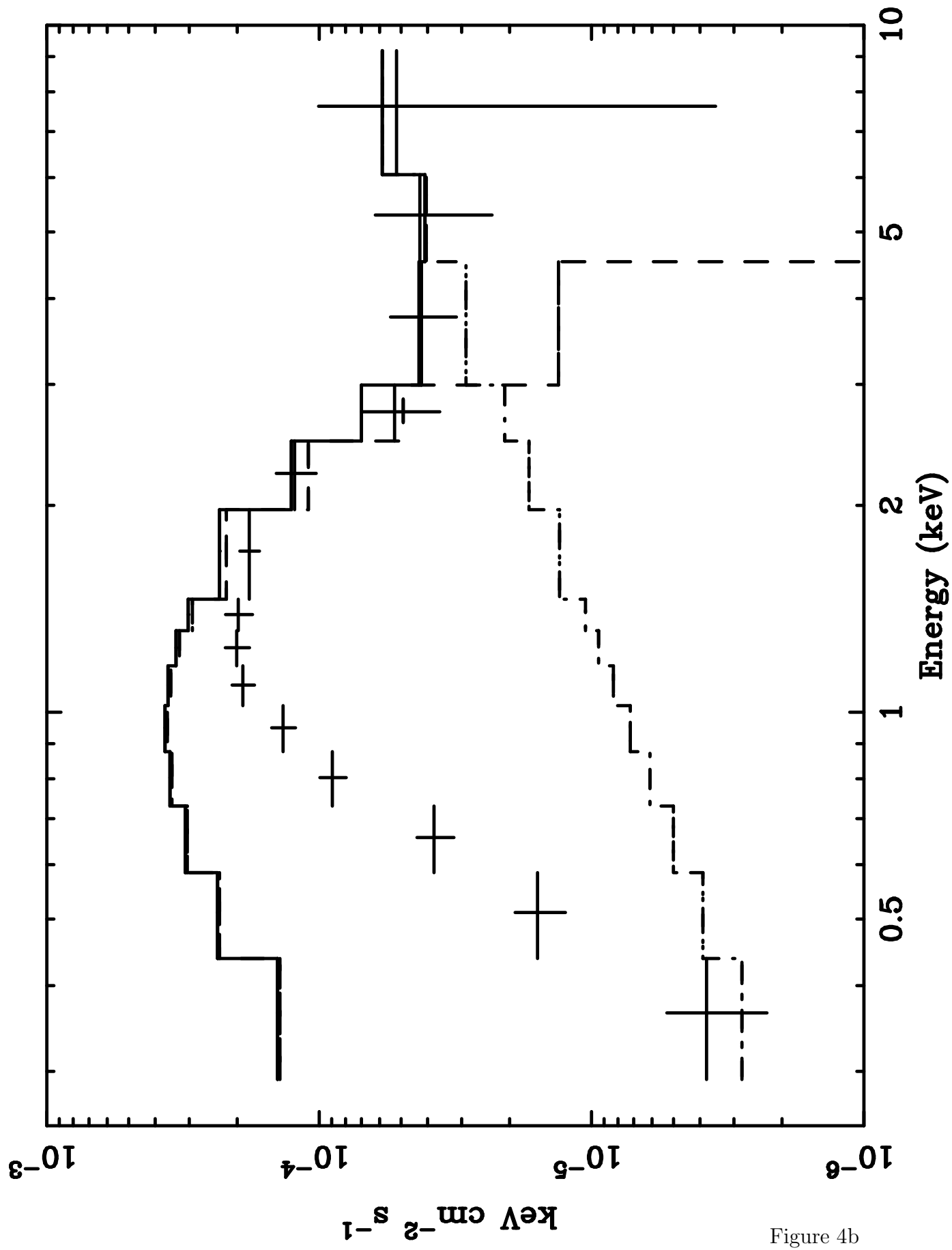
Figure 4b

Aql X−1, Mar 23 2001: Chandra ACIS−S/BI

Energy (keV)

keV cm^{-2} s^{-1}
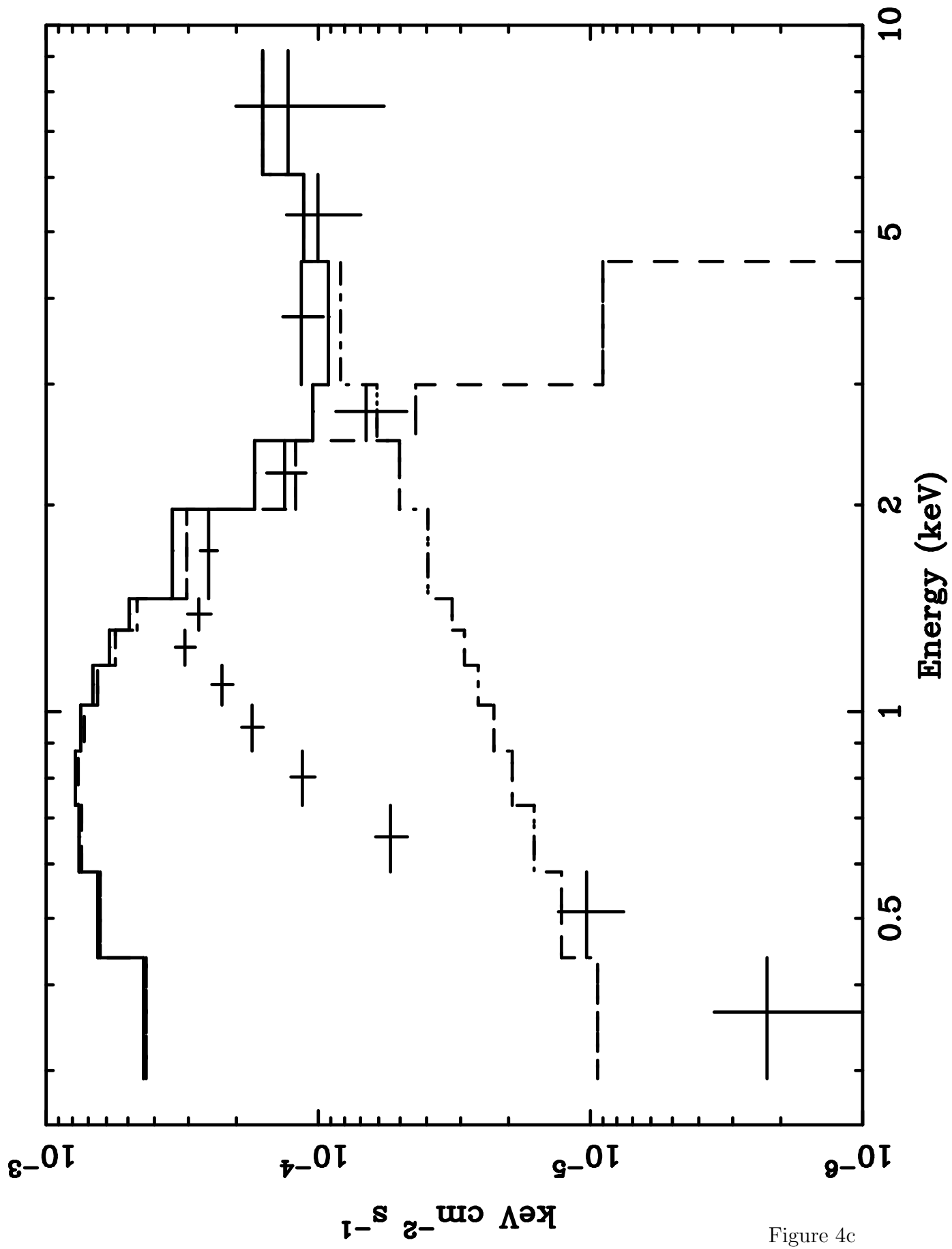
Figure 4c

Aql X-1, Apr 20 2001: Chandra ACIS-S/BI

keV cm^{-2} s^{-1}

Energy (keV)
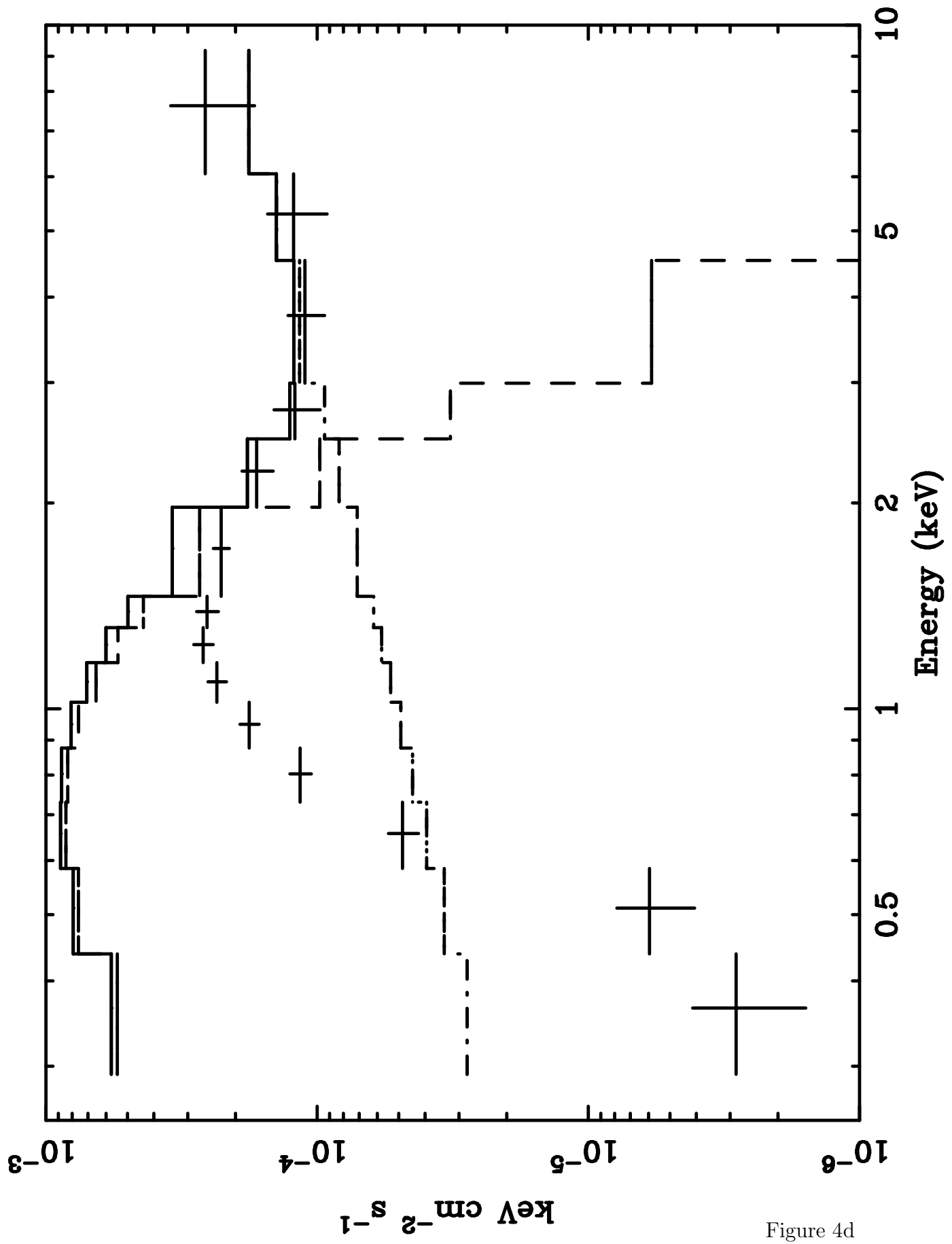
Figure 4d

Aql X-1: Chandra ACIS-S/BI (0.3-9.0 keV); Obs. #3 and #4

Figure 5

Figure 6

Figure 7

E0102-72.3

counts/sec/kev

ratio

channel energy (keV)
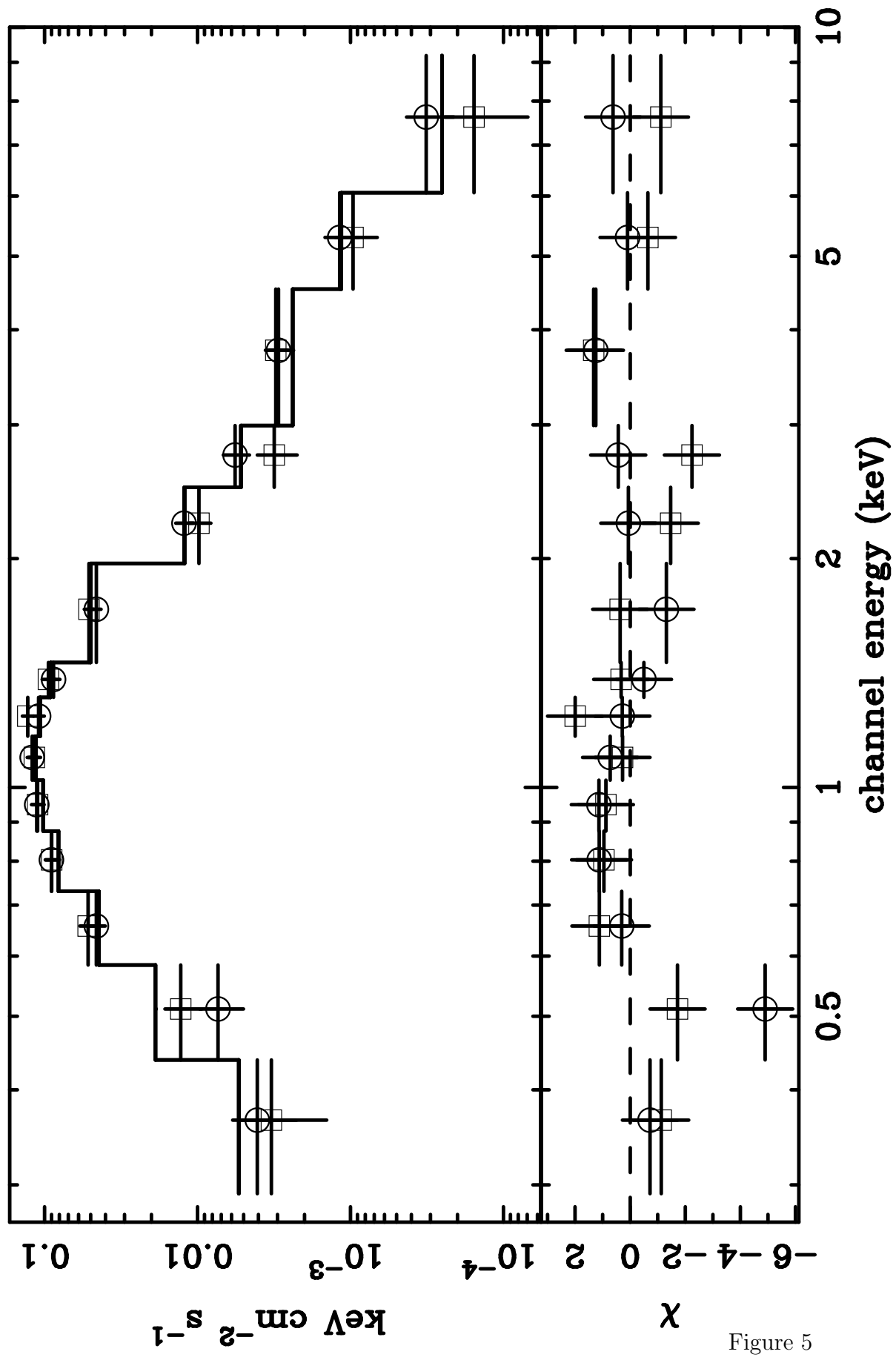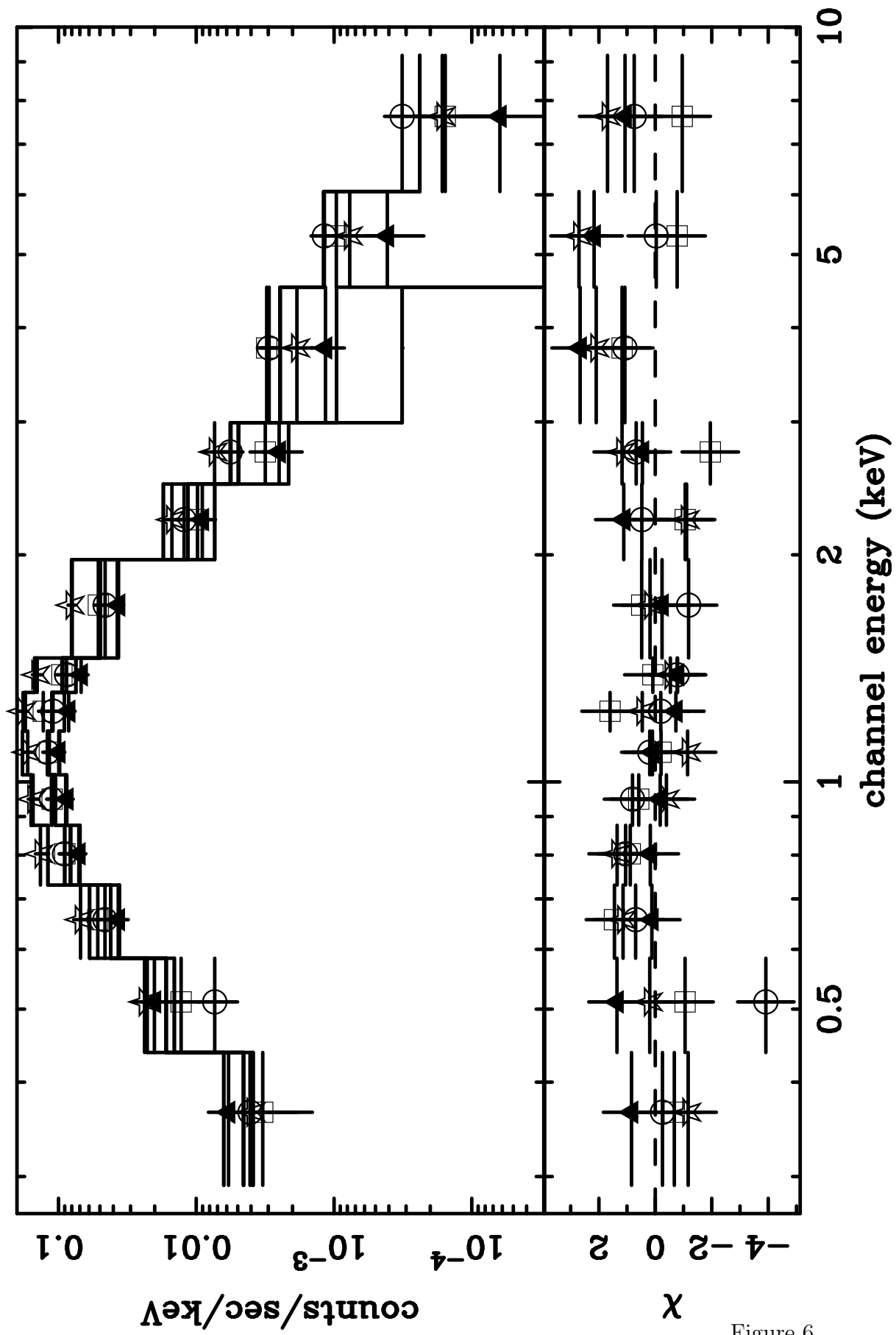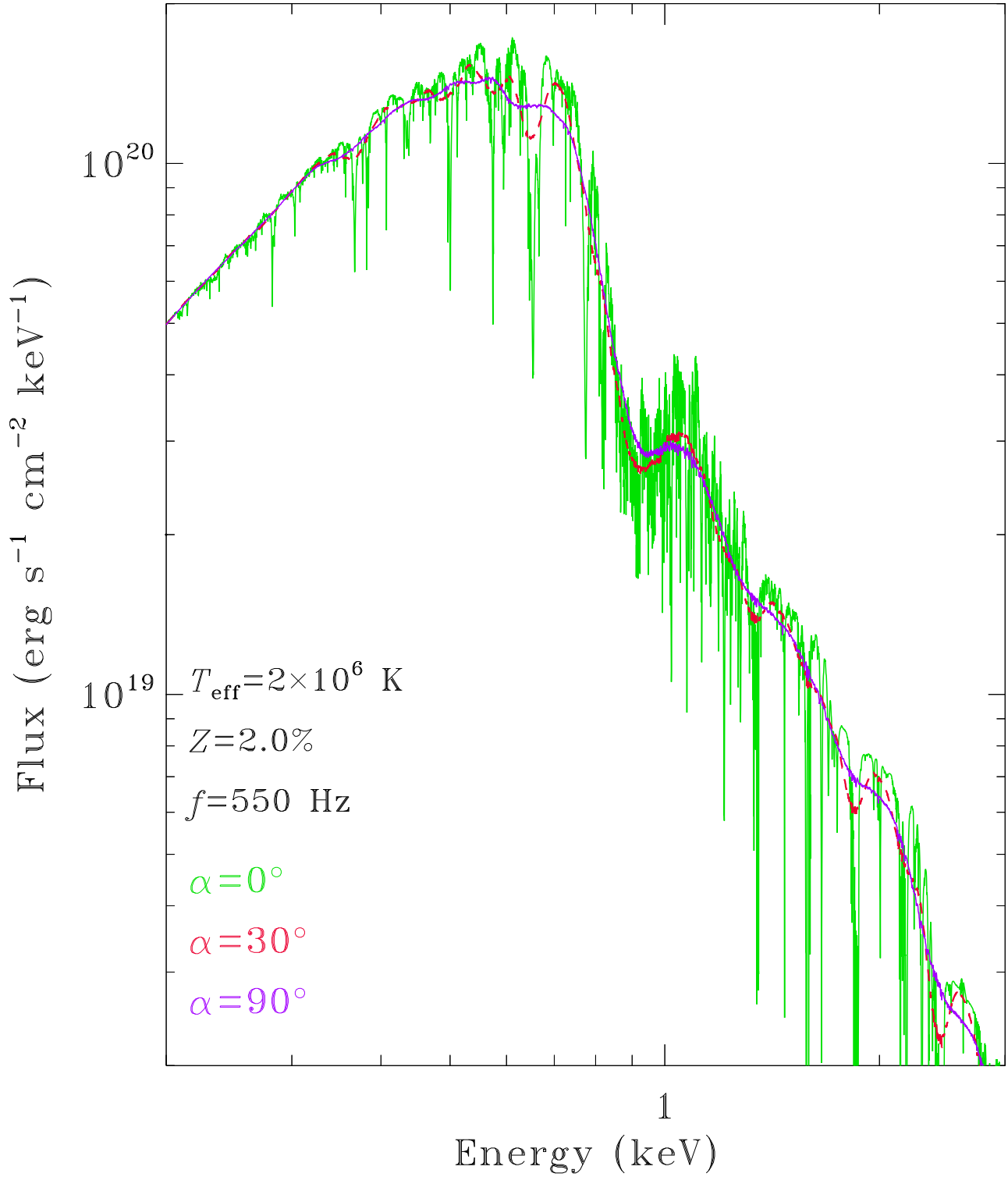
Figure 8
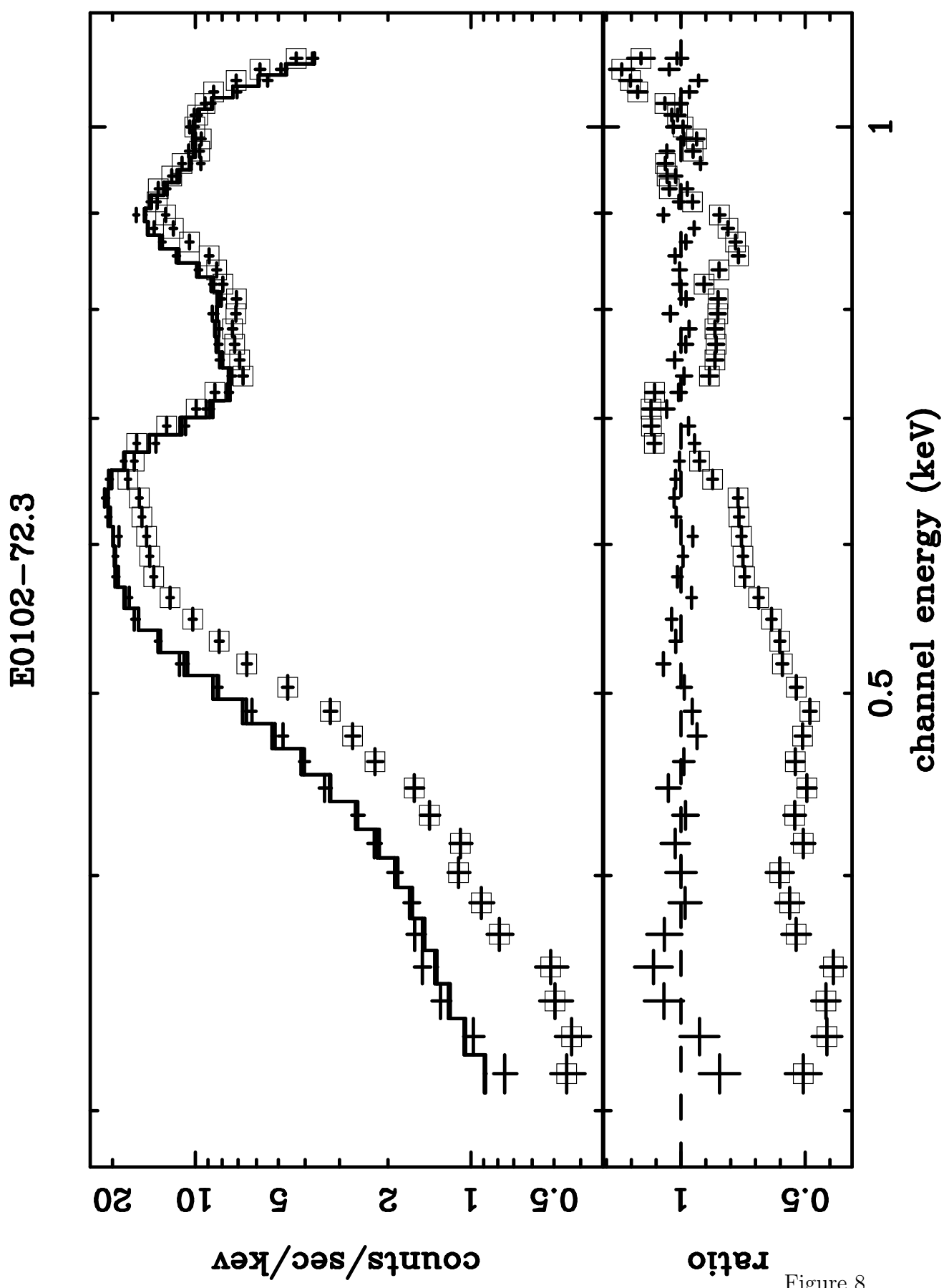
Table 1.   Log of *Chandra*/ACIS-S Observations

Obs #	Start Time (TT)	Exposure (sec)	c/ksec (0.5-10 keV)	c/ksec (0.3-1.0 keV)	c/ksec (1.0-2.5 keV)	c/ksec (2.5-8 keV)	Orbital Phase[a] ϕ_{orb}
1	2000-11-28 10:52:39	6628	183±5	56±3	120±4	8.3±1.1	0.02–0.15 (±0.01)
2	2001-02-19 11:25:52	7787	94±3	32±2	60±3	3.9±0.7	0.20–0.36 (±0.02)
3	2001-03-23 20:09:11	7390	127±4	39±3	81±3	8.2±1.1	0.19–0.34 (±0.02)
4	2001-04-20 11:53:32	9245	123±4	38±2	76±3	9.9±1.0	0.22–0.39 (±0.02)

Note. — [a] Orbital phase relative to minimum light (inferior conjunction of the secondary), ephemeris from Garcia & Callanan (1999), orbital period from Chevalier & Ilovaisky (1998a)

Table 2.   Intensity Variability

Obs. #	α	Total Counts	RMS (%)
1	(1.8)	1237	<18
2	(1.8)	755	<26
3	(1.8)	956	<29
4	1.8±0.4	1161	32^{+8}_{-6}

Note.   — Values in parenthesis are fixed. RMS is percentage root mean square variability, integrated between 0.0001-1 Hz, in excess of the Poisson level; error bars are 1σ, upper-limits are 3σ.

Table 3. *Chandra* Best-Fit Spectral Parameters for Individual Observations

Obs. #	$N_{\mathrm{H},22}$	$kT_{\mathrm{eff},\infty}$ (eV)	R_∞ (km/(D/ 5 kpc))	α	N_{pl} ()	f_{pl} (%)	Flux[a] (0.5-10 keV)	χ^2_ν (prob)
1	0.46 ± 0.04	118^{+8}_{-6}	20^{+5}_{-3}	(1.0)	$<2\times10^{-5}$	$<17\%$	18	0.83/10 (0.07)
2	0.37 ± 0.06	120 ± 20	13^{+6}_{-4}	(1.0)	$<1.2\times10^{-5}$	$<22\%$	8	0.24/9 (0.99)
3	$0.58^{+0.06}_{-0.10}$	83^{+19}_{-13}	44 ± 17	1.2 ± 0.6	$3^{+5}_{-2}\times10^{-5}$	18%	19	0.98/9 (0.45)
4	$0.66^{+0.04}_{-0.09}$	67^{+11}_{-11}	80^{+44}_{-33}	1.9 ± 0.5	$1^{+1}_{-0.5}\times10^{-5}$	24%	23	1.3/9 (0.25)

Note. — [a] X-ray fluxes are corrected for galactic absorption, in units of 10^{-13} erg cm^{-2} s^{-1} (0.5-10 keV). N_{pl} is the power-law component normalization in phot keV^{-1} cm^{-2} s^{-1} at 1 keV. f_{pl} is the fraction of the the Total Model Flux which is accounted for by the power-law component (these are typically uncertain by 50-100%). Upper-limits are 90% confidence, uncertainties are 1σ. Values in parenthesis are held fixed. Assumed source distance D=5 kpc.

Table 4. N_{H} in the direction of Aql X-1

Ref.	Method	Value
Callanan et al. (1999)	Optical Photometry	0.29 ± 0.06
Dickey & Lockman (1990) (W3NH)	Weighted average integrated 21 cm emission	0.34 ± 0.01
Thorstensen et al. (1978)	Optical Photometry of nearby B star	0.40
Obs. 1+2[a] (0.3-9 keV)	X-ray spectral modelling	0.43 ± 0.03
Obs. 3+4[a] (0.3-9 keV)	X-ray spectral modelling	0.61 ± 0.06

Note. — The value for observations 3+4, without accounting for the apparent 0.45-0.6 keV deficit, appears discrepant

Table 5.   Spectral Parameters for Observations 1+2 and 3+4

Obs. #	$N_{\rm H,22}$	$kT_{\rm eff,\infty}$ (eV)	R_∞ (km/(D/ 5 kpc))	α	N_{pl} (phot/cm^{-2}s^{-1} 1 keV)	f_{pl} (%)	χ^2_ν (prob)
. . . . Observations 1+2; $N_{\rm H}$ varies							
1	n/a	n/a	n/a	n/a	n/a	n/a	5.0/22 (1×10^{-13})
2	n/a	"	"	n/a	n/a	n/a	"
. . . . Observations 1+2; R_∞ varies							
1	0.41±0.03	122^{+11}_{-9}	18.0±3.5	0.4±0.9	$<4.5\times10^{-5}$	<11	0.83/22 (0.69)
2	"	"	12.9±2.6	"	"	<21	"
. . . . Observations 1+2; $kT_{\rm eff,\infty}$ varies							
1	0.43±0.03	125^{+12}_{-9}	$17.2^{+2.6}_{-3.6}$	0.9±1.0	$<9\times10^{-5}$	<21	0.67/22 (0.87)
2	"	108^{+11}_{-7}	"	"	"	<35	"
. . . . Observations 1+2; $F_{X,pl}$ varies							
1	0.83±0.04	(115)	$R_\infty<7.1$	4.5±0.2	(2.1±0.3)×10^{-3}	>97	1.2/22 (0.36)
2	"	"	"	"	(1.1±0.2)×10^{-3}	>95	"
. . . . Observations 3+4							
3+4	0.60±0.05	81±12	46^{+23}_{-11}	1.5±0.5	(5±2)×10^{-5}	21	1.2/23 (0.25)
3+4	(0.43)	113±1	(17.2)	0.8±0.3	$(1.7^{+1.0}_{-0.7})\times10^{-5}$	26	1.71/25 (0.015)
3+4[b]	(0.43)	114±1	(17.2)	0.7±0.4	$(1.5^{+1.1}_{-0.7})\times10^{-5}$	26	0.76/23 (0.78)

Note. — Uncertainties are 1σ, upper-limits are 90% confidence. Assumed distance is 5 kpc(Rutledge et al. 2001a). Notation "n/a" (not applicable) is used where spectral parameters were used in a fit which is not statistically acceptable. Upper-limits on f_{pl}, the fraction of the 0.5-10.0 unabsorbed flux due to the power-law component, were derived from the best-fit model for the normalization N_{pl} held fixed its 90% confidence limit.

Table 6.   Joint Spectral Parameters (Observations 1-4)

Obs. #	$N_{\mathrm{H},22}$	$kT_{\mathrm{eff},\infty}$ (eV)	R_∞ (km/(D/ 5 kpc))	α	N_{pl} (phot/cm^{-2}s^{-1} 1 keV)	f_{pl} (%)	χ^2_ν (prob)
Observations 1-4 (0.6-9.0 keV); $kT_{\mathrm{eff},\infty}$ varies
1	0.42±0.03	121^{+13}_{-6}	$18.4^{+0.4}_{-3.8}$	$1.1^{+0.2}_{-0.6}$	$(1.7^{+1.4}_{-0.9})\times10^{-5}$	13	1.0/41 (0.40)
2	”	105^{+9}_{-6}	”	”	”	23	”
3+4	”	110^{+12}_{-5}	”	”	”	19	”
Observations 1-4 (0.6-9.0 keV); N_{H} varies
1	n/a	n/a	n/a	n/a	n/a	n/a	3.0/41 (2×10^{-10})
2	n/a	”	”	”	“	“	”
3+4	n/a	”	”	”	“	“	”
Observations 1-4 (0.6-9.0 keV); R_∞ varies
1	0.39^{+5}_{-3}	122^{+13}_{-17}	$17.6^{+4.3}_{-2.5}$	$0.7^{+0.5}_{-0.3}$	$(0.8^{+1.4}_{-0.4})\times10^{-6}$	13	1.13/41 (0.26)
2	”	“	$12.5^{+3.1}_{-1.8}$	”	”	23	”
3+4	”	“	$14.3^{+1.6}_{-2.1}$	”	”	18	”
Observations 1-4 (0.6-9.0 keV); $F_{X,pl}$ varies
1	n/a	n/a	n/a	n/a	n/a	n/a	1.60/41 (0.0085)
2	”	”	”	”	n/a	n/a	”
3+4	”	”	”	”	n/a	n/a	”
Observations 1-4 (0.6-9.0 keV); α and $F_{X,pl}$ vary
1	0.52±0.04	88^{+10}_{-7}	32.5^{+4}_{-4}	3.2±0.2	$(4.5±0.5)\times10^{-4}$	54	1.08/39 (0.34)
2	”	”	”	1.0±0.7	$(9^{+17}_{-6})\times10^{-6}$	10	”
3+4	”	”	”	2.0±0.3	$(9.5±3)\times10^{-5}$	30	”
Observations 1-4 (0.6-9.0 keV); N_{H} and α fixed, all other values vary
1	(0.34)	142^{+4}_{-3}	$11.9^{+0.2}_{-0.3}$	(1.0)	<1.6×10^{-5}	<16	0.73/41 (0.89)
2	”	122^{+4}_{-3}	”	“	<1.1×10^{-5}	<20	”
3+4	”	128±4	”	“	$(2.0^{+0.4}_{-0.1})\times10^{-5}$	28^{+6}_{-3}	”
Observations 1-4 (0.6-9.0 keV); kT_{eff} varies, N_{H} and R_∞ fixed
1	(0.34)	138±1	(13.0)	0.6±0.4	(0)	(0)	1.30/43 (0.11)
2	”	120±1	”	”	(0)	(0)	”
3+4	”	124^{+1}_{-2}	”	”	$(1.1^{+1.5}_{-0.3})\times10^{-5}$	29	”
Observations 1-4 (0.3-9.0 keV); kT_{eff} varies, N_{H} and R_∞ fixed
1	(0.34)	n/a	(13.0)	n/a	(0)	(0)	2.63/51 (2×10^{-9})
2	”	n/a	”	”	(0)	(0)	”
3+4	”	n/a	”	”	n/a	n/a	”
Observations 1-4 (0.3-9.0 keV); kT_{eff} varies, N_{H} and R_∞ float
1	n/a	n/a	n/a	n/a	(0)	(0)	1.62/49 (0.0038)
2	”	n/a	”	”	(0)	(0)	”
3+4	”	n/a	”	”	n/a	n/a	”
^{a} Observations 1-4 (0.3-0.45, 0.6-9.0 keV); kT_{eff} varies, N_{H} and R_∞ float
1	$0.42^{+0.02}_{-0.03}$	130^{+3}_{-5}	$15.9^{+0.8}_{-2.9}$	0.7±0.2	(0)	(0)	1.26/48 (0.105)
2	”	113^{+3}_{-4}	”	”	(0)	(0)	”
3+4	”	118^{+9}_{-4}	”	”	$(1.4^{+0.9}_{-0.8})\times10^{-5}$	26	”
Observations 1-4 (0.3-9.0 keV); kT_{eff} varies, N_{H} and R_∞ float
1	n/a	n/a	n/a	n/a	(0)	(0)	1.66/47 (0.0030)
2	n/a	n/a	”	”	(0)	(0)	”
3+4	n/a	n/a	”	”	n/a	n/a	”

Note. — ^{a} See Table 7 for luminosities derived from these values. ^{b}. The 0.45-0.6 keV band is excluded from the data fit with these models. Uncertainties are 1σ, upper-limits are 90% confidence. Assumed distance is 5 kpc(Rutledge et al. 2001a). Notation "n/a" (not applicable) is used where spectral parameters were used in a fit which is not statistically acceptable. Upper-limits on f_{pl}, the fraction of the 0.5-10.0 unabsorbed flux due to the power-law component, were derived from the best-fit model for the normalization N_{pl} held fixed its 90% confidence limit.

Table 7.   X-ray Luminosities

Obs.	Thermal L_x	Total L_x
1	4.6	4.6
2	2.5	2.5
3+4	3.0	4.0

Note. — Assumed source distance d=5 kpc. Luminosities are corrected for absorption, in units of 10^{33} erg s^{-1}, 0.5-10 keV.

Table 8.   Observed vs. Best-Fit Model Counts in 0.45-0.6 keV Bin

Obs.(i)	Observed Counts (x_i)	Model Counts (μ_i)
1	23	26.0
2	23	19.5
3	13	21.4
4	10	26.7

Note. — Best-Fit Model parameters used to derive these values are in Table 6; the best-fit model for observations 1-4, using 0.3-9.0 keV, ignoring 0.45-0.6 keV, permitting $kT_{\mathrm{eff},\infty}$ to vary between observations, and N_{H} and R_∞ to be the same between observations. Best fit χ^2_ν=1.26/48 dof, prob=0.105.

Aql X-1, Obs. #1-4: Chandra ACIS-S/BI

Energy (keV)

keV cm^{-2} s^{-1}